ACS NANO

www.acsnano.org

ARTICLE

Achieving Fast and Durable Lithium Storage through Amorphous FeP Nanoparticles Encapsulated in Ultrathin 3D P-Doped Porous Carbon Nanosheets

Zhiming Zheng,[▽] Hong-Hui Wu,[▽] Haodong Liu, Qiaobao Zhang,* Xin He, Sicen Yu, Victoria Petrova, Jun Feng, Robert Kostecki, Ping Liu, Dong-Liang Peng, Meilin Liu, and Ming-Sheng Wang*

Cite This: *ACS Nano* 2020, 14, 9545–9561

Read Online

ACCESS | Metrics & More | Article Recommendations | Supporting Information

ABSTRACT: Conversion-type transition-metal phosphide anode materials with high theoretical capacity usually suffer from low-rate capability and severe capacity decay, which are mainly caused by their inferior electronic conductivities and large volumetric variations together with the poor reversibility of discharge product (Li_3P), impeding their practical applications. Herein, guided by density functional theory calculations, these obstacles are simultaneously mitigated by confining amorphous FeP nanoparticles into ultrathin 3D interconnected P-doped porous carbon nanosheets (denoted as FeP@CNs) *via* a facile approach, forming an intriguing 3D flake-CNs-like configuration. As an anode for lithium-ion batteries (LIBs), the resulting FeP@CNs electrode not only reaches a high reversible capacity (837 mA h g^{-1} after 300 cycles at 0.2 A g^{-1}) and an exceptional rate capability (403 mA h g^{-1} at 16 A g^{-1}) but also exhibits extraordinary durability (2500 cycles, 563 mA h g^{-1} at 4 A g^{-1}, 98% capacity retention). By combining DFT calculations, *in situ* transmission electron microscopy, and a suite of *ex situ* microscopic and spectroscopic techniques, we show that the superior performances of FeP@CNs anode originate from its prominent structural and compositional merits, which render fast electron/ion-transport kinetics and abundant active sites (amorphous FeP nanoparticles and structural defects in P-doped CNs) for charge storage, promote the reversibility of conversion reactions, and buffer the volume variations while preventing pulverization/aggregation of FeP during cycling, thus enabling a high rate and highly durable lithium storage. Furthermore, a full cell composed of the prelithiated FeP@CNs anode and commercial $LiFePO_4$ cathode exhibits impressive rate performance while maintaining superior cycling stability. This work fundamentally and experimentally presents a facile and effective structural engineering strategy for markedly improving the performance of conversion-type anodes for advanced LIBs.

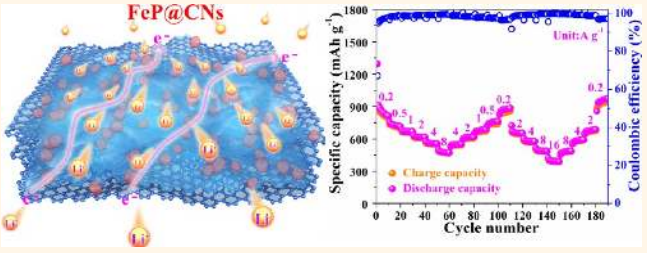

KEYWORDS: *amorphous FeP, carbon nanosheets, in situ TEM, anode materials, lithium ion batteries*

Given the merits of high energy density and long cycle life, lithium-ion batteries (LIBs) will continue to play a vital role as the dominant power source for mobile electronic devices and electric vehicles.[1−11] However, commercially used graphitic anodes in LIBs with limited theoretical capacity (~370 mA h g^{-1}) cannot meet the ever-increasing demands of high energy densities for electric vehicles and grid-scale energy storage systems.[12−16] Therefore, the key for achieving high-energy LIBs is to seek promising anode candidates to substitute conventional graphite. Transition-metal compounds with conversion-type reaction mechanisms, including oxides,[17−23] sulfides,[24−26] and phosphides,[27−29] have thus been extensively investigated as alternative anodes for LIBs due to their ability to provide high capacity from multiple electron transfers per metal center. Among these anode materials, transition-metal phosphides (TMPs) stand out as they display lower polarization and a more favorable potential for lithium storage together with a higher specific capacity, making them more suitable as

Received: October 30, 2019
Accepted: July 13, 2020
Published: July 13, 2020

https://dx.doi.org/10.1021/acsnano.9b08575
ACS Nano 2020, 14, 9545–9561

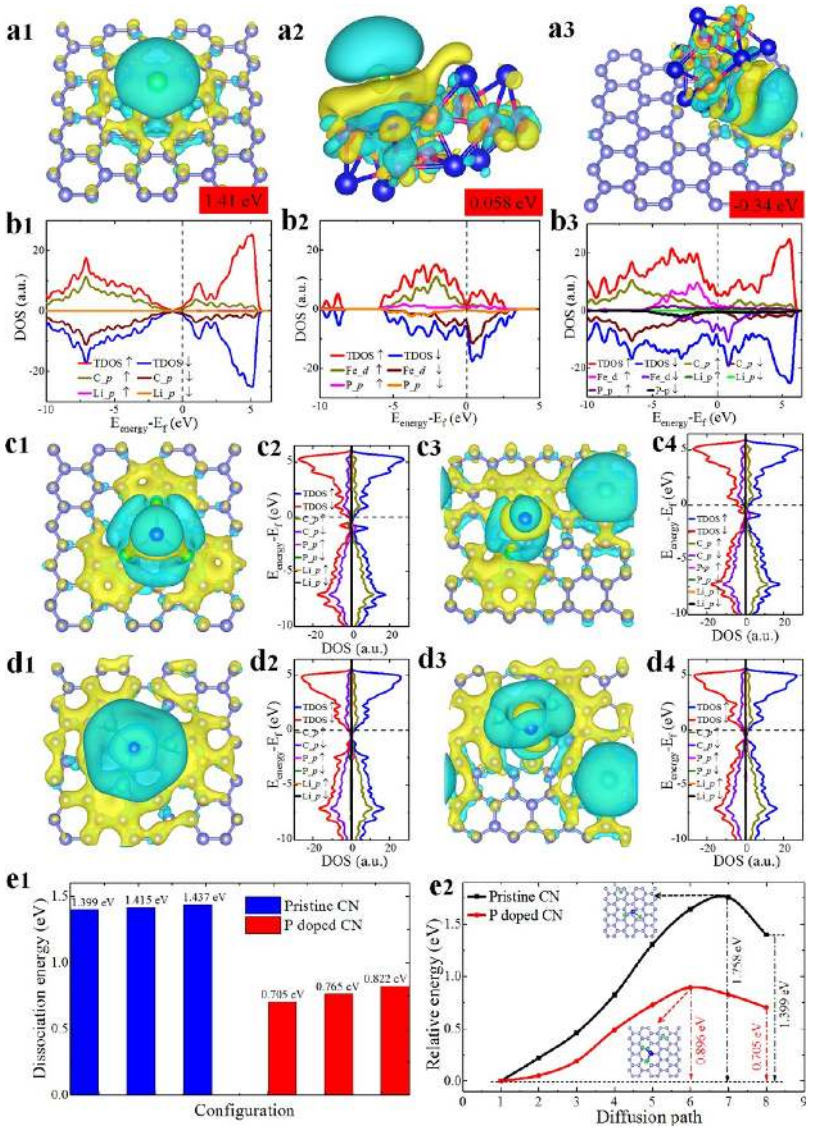

Figure 1. Theoretical roadmap for an advanced Li-ion battery anode. (a1)−(a3) 3D charge difference of the pristine CN, FeP particle, and FeP@CN adsorbing one Li; (b1)−(b3) corresponding PDOS and TDOS; (c1) Li_3P adsorbed on CN, (c2) corresponding DOS, (c3) Li_2P+Li adsorbed on CN, (c4) corresponding DOS; (d1) Li_3P adsorbed on P-doped CN, (d2) corresponding DOS, (d3) Li_2P + Li adsorbed on P doped CN, (d4) the corresponding DOS; (e1) the dissociation energy of three configurations of Li_3P adsorbed on CN, and three configurations of Li_3P adsorbed on P-doped CN,(e2) the energy path of the dissociation from Li_3P to Li_2P + Li. The slate blue, blue, red, and green balls represent C, P, Fe, and Li atoms, respectively.

anodes.[15,16,30,31] Unfortunately, less attention has been devoted to exploring TMPs, probably because they are more difficult to synthesize than other anodes.[15,16] The present synthetic route for most reported TMPs is generally conducted by using a high boiling point organic phosphorus source in the oil phase under an inert protective atmosphere.[16] This may cause the reaction to be corrosive and flammable under high decomposition temperatures (300 °C), and these long-chain organic solvents are also difficult to wash away. Another common method for preparing TMPs utilizes the generated PH_3 from the decomposition of upstream sodium hypophosphite (NaH_2PO_2) carried by protective gas flow (Ar or N_2) and reacted with various TM precursors (metal oxides, hydroxides, metal−organic frameworks, *etc.*).[15,32] The reaction appears to be facile and the generated byproduct Na_2HPO_4 in the upstream is easily washed away, but the main problem is that PH_3 is extremely toxic and lethal even at a few ppm. The obvious shortcomings of these strategies lie in the procedure and inevitably increase environmental damage, raise the preparation cost, and complicate the synthesis processes.[33] In this regard, suitable and viable strategies for fabricating TMPs are urgently needed.

It is also worth noting that although TMPs have high theoretical capacities and low redox voltages, there are still a few challenges when it comes to the practical applications of these TMPs, namely, poor rate capability and severe capacity decay, which are caused by their inferior electrical conductivity and drastic volume variation during cycling as well as poor reversibility of discharge product (Li_3P).[15,16,34−36] To resolve these challenges, one effective strategy toward improving cycling stability and rate performance is to integrate nanostructured TMPs with a conductive carbon (C) component forming TMPs@ C hybrid structures.[15,36−40] Some examples of TMPs@C hybrid structures have been proven to enhance

https://dx.doi.org/10.1021/acsnano.9b08575
ACS Nano 2020, 14, 9545−9561

electrochemical performance, including GeP_5@C composites,[41] ZnP_2@graphite composites,[42] graphene@Ni_2P hybrids,[38] CoP nanocubes/graphene composites,[43] and Sn_4P_3@C composites,[44,45] *etc*. Despite these advances, the reversible capacity and structural integrity of the electrode during the cycling process, especially at higher rates, is still unsatisfactory and needs to be addressed.[15,34] It is thus highly desirable, yet quite challenging, to develop a convenient but effective strategy of constructing TMPs@C hybrid structures with the ultimate aim of improving the ion and electron transport, buffering the volume variations and maintaining the integrity of the electrode microstructure during cycling through purposeful design to further improve their electrochemical performance. Additionally, underlying fundamental mechanisms and interplays between TMPs and C components on performance enhancement remain to be further investigated.

Herein, informed by density functional theory (DFT) calculations, we demonstrate a perspective of encapsulating amorphous FeP nanoparticles into a 3D interconnected P-doped porous C nanosheets (denoted as FeP@CNs) to form a 3D flake-CNs-like configuration as efficient anodes for LIBs, which are synthesized *via* a facile and viable approach involving a simple ultrasonic dispersion and subsequent heat treatment under an argon atmosphere. This intriguing architectural design integrates nanostructured amorphous FeP and 3D porous microstructures of CNs and offers several favorable design attributes for high performance, as elaborated by DFT calculations and experimental investigations. Specifically, the existence of coupling between FeP- and P-doped CNs associated with the P doping in CNs can facilitate the sturdy contact of the hybrid with enhanced conductivity and adsorption abilities for FeP and Li^+ and boost the reversibility of discharge product Li_3P by reducing its dissociation energies, as predicted by DFT results. The amorphous structure of FeP could dramatically reduce the risk of fracture during cycling, profiting from isotropic stress,[42] whereas the nanoscale of the FeP shortens the electron and ion transport path.[16] The 3D porous interconnected CNs framework can provide a buffer matrix for alleviating the structural strain and accommodating the volume variations of active FeP during cycling, as proven directly by *in situ* and *ex situ* transmission electron microscopy (TEM) observations, giving rise to long-term stabilization.[36,46] Meanwhile, the open porous structure and interconnected network of the CNs can offer unobstructed channels for fast ion and electron transport and a structural scaffold to prevent embedded FeP from aggregating, resulting in an ultrahigh rate capacity with excellent cycle stability.[46−48] With these merits, the resulting FeP@CNs electrodes promise extraordinary lithium storage performance in terms of high reversible capacity, exceptional rate capability, and ultralong cycling life, which outperformed many reported results of TMP-, TMO-, and TMS-based composite anodes. Impressively, they also display superior sodium-ion storage properties, namely, outstanding rate capability and long-life cycling stability. The full cell comprising of prelithiated FeP@CNs as anode and $LiFePO_4$ as cathode shows outstanding cycling stability with 89.2% capacity retention after 100 cycles at 1C while maintaining impressive rate capability. The demonstrated design strategy and fundamental insights obtained from our work would render opportunities to develop high-performance and durable anodes for next-generation LIBs as well as other rechargeable batteries.

RESULTS AND DISCUSSION

To gain insight into the performance of FeP particles on the P-doped CN (simplified as FeP@CN) composite from the electronic and atomic scale, DFT calculations are first carried out to explore the adsorption energy, electronic structure, dissociation energy, and energy paths of the dissociation process of discharge products Li_3P. Parts a1−a3 of Figure 1 show the 3D charge difference and adsorption energy of the optimized pristine CN, bare FeP particle, and FeP@CN adsorbing a single Li atom, respectively. It is found that the distribution of charge difference of the FeP particle and FeP@CN adsorbing a Li is much more localized than the pristine CN adsorbing a Li. Although the total charge transfer of the Li atom on pristine CN is slightly larger than that of the Li atom the FeP particle and FeP@CN (Bader analysis in Supplementary Table S1), considering the localized nature of FeP@CN adsorbing one Li atom, the best adsorption energy is obtained with FeP@CN (−0.34 eV, and the Li atom on pristine CN and FeP particle are 1.41 and 0.058 eV, respectively). The energy landscape and diffusion path of Li^+ on the FeP surface are shown in Figure S1. As shown, the energy barriers between three minimum sites are 0.42 and 0.41 eV, respectively. The low-energy barrier of Li^+ diffusion from DFT is comparable to the reported values for $LiMnPO_4$ (0.60 eV),[49] $Bi_2M_oO_6$ (0.40 eV),[50] Bi_2S_3 (0.57 eV),[51] and $LiFePO_4$,[49] and it indicates a fast rate of Li^+ diffusion. To confirm the coupling between P doped CN and FeP, we calculate the charge difference of FeP on P doped CN, it is found that the coupling is very localized to the interface. The Bader charge is 0.195 e transferring from the FeP to the P doped CN, and the binding energy of the FeP and P doped CN is −2.807 eV, indicating a strong coupling between P doped CN and FeP in the composite. The 3D charge differences of FeP on the P doped CN is shown in Figure S2. The corresponding partial density of states (PDOS) and total density of states (TDOS) are calculated based on the electron structure and bonding, and the dominating valence electron states for different atoms (*p* states for C, P, Li and *d* states for Fe) are shown in parts b1−b3, respectively, of Figure 1. As compared to that of their components (CN and FeP particle), an exponential increase of the electronic states is achieved for the FeP@CN near Fermi level from the valence electron states of C, P, Fe, and Li. It is evidently observed that that the coupling between P-doped CN and FeP particles strongly influences the electronic structures of both CN and FeP particles, thereby improving the overall electronic conductivity of the whole coupled system. This favors efficient electron transport and provides rapid reaction kinetics and more charge storage sites for both FeP- and P-doped CN, accounting for high capacity and rate performance evidenced by electrochemical results.

The 3D charge differences of Li_3P and Li_2P + Li on the pristine CN are given in parts c1 and c3, respectively, of Figure 1. It is found that the charge difference between Li_3P and CN is more localized than that of Li_2P + Li with CN. As shown in Table S1, detailed Bader charge analysis also suggests that the corresponding charge transfer of P atom is reduced from 1.618 to 1.245 e during the dissociation process from Li_3P to Li_2P + Li. The 3D charge differences of Li_3P and Li_2P + Li on the P-doped CN are given in parts d1 and d3, respectively, of Figure 1. It demonstrates that the charge difference on P-doped CN is less localized than that on pristine CN. The Bader charge analysis also shows that the total charge transfers of the

https://dx.doi.org/10.1021/acsnano.9b08575
ACS Nano 2020, 14, 9545−9561

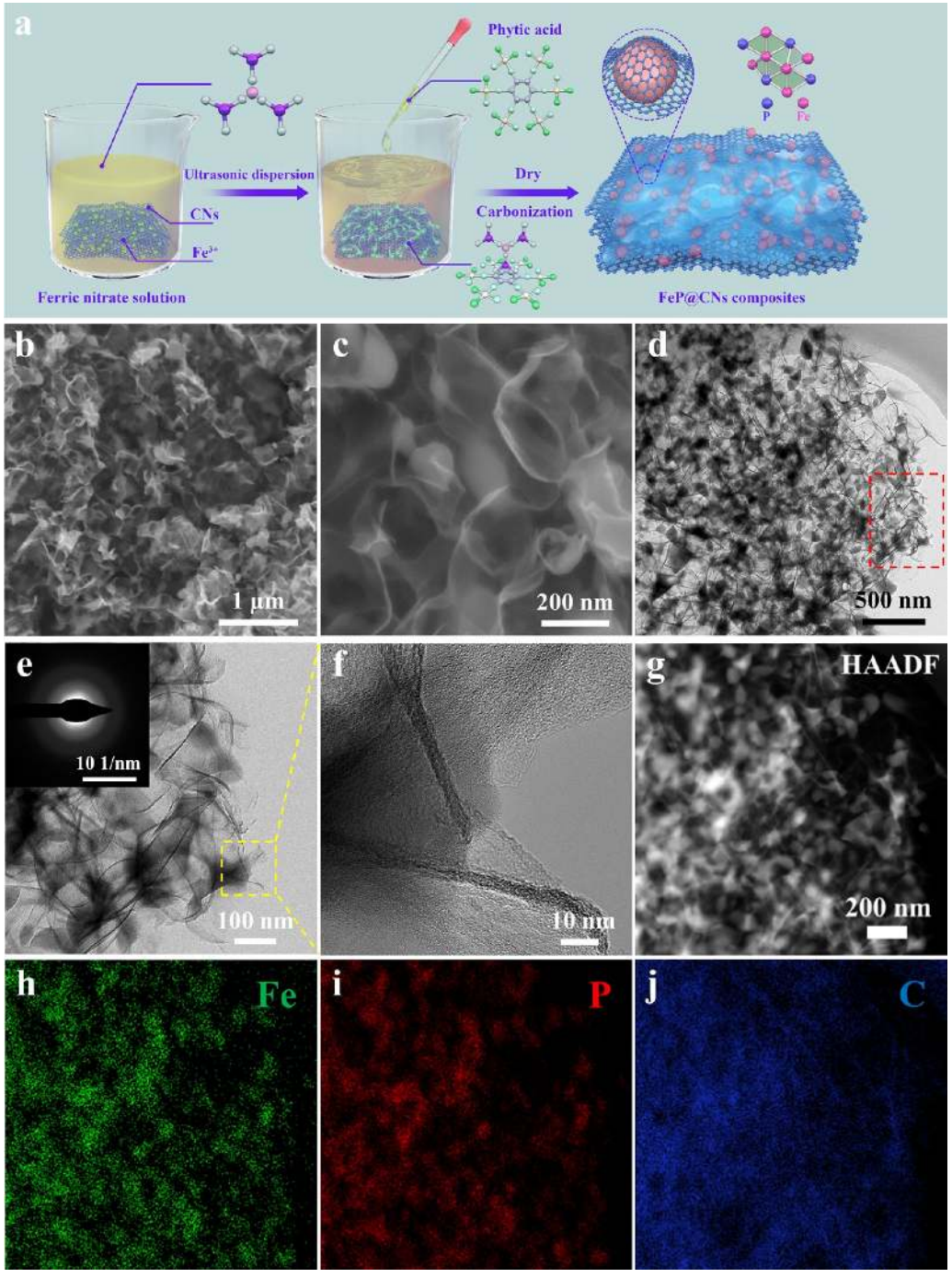

Figure 2. (a) Schematic drawing of fabricating the FeP@CNs composite and (b, c) FESEM images of FeP@CNs. (d, e) TEM and (f) HRTEM (the inset in Figure 2e shows the corresponding SAED image) image of FeP@CNs composite. (g) HAADF image of FeP@CNs and corresponding element mappings of (h) Fe, (i) P, and (j) C elements.

adsorbed P atom of the Li_3P and Li_2P + Li on P-doped CN are reduced to 1.132 and 0.904 e, respectively. The corresponding DOS, given in parts e2, e4, d2, and d4, respectively, of Figure 1, suggest all of the configurations show metallic features, indicating excellent conductivity. The corresponding atomic configurations without charge difference plots are presented in Figure S3. The dissociation energy of three configurations of $Li_3P \rightarrow Li_2P$ + Li adsorbed on CN, and three configurations of $Li_3P \rightarrow Li_2P$ + Li adsorbed on P doped CN are summarized in Figure 1e1. These results demonstrate that the dissociation energy of $Li_3P \rightarrow Li_2P$ + Li are significantly reduced with the presence of the P doping (reduced from 1.399 to 0.705 eV), indicating an excellent catalytic effect, which can be well explained by the smaller charge transfer value of Li_3P/Li_2P + Li on P-doped CN than that on pristine CN (Supplementary Table S1). Figure 1e2 presents the energy path of the dissociation from Li_3P to Li_2P + Li, it also suggests a lower energy barrier of $Li_3P \rightarrow Li_2P$ + Li on P doped CN (0.896 eV) than that on pristine CN (1.758 eV). Therefore, it can be inferred that the doping of P into CN could be a promising strategy to boost the reversibility of Li_3P, which thereafter verified by *ex situ* TEM results.

https://dx.doi.org/10.1021/acsnano.9b08575
ACS Nano 2020, 14, 9545−9561

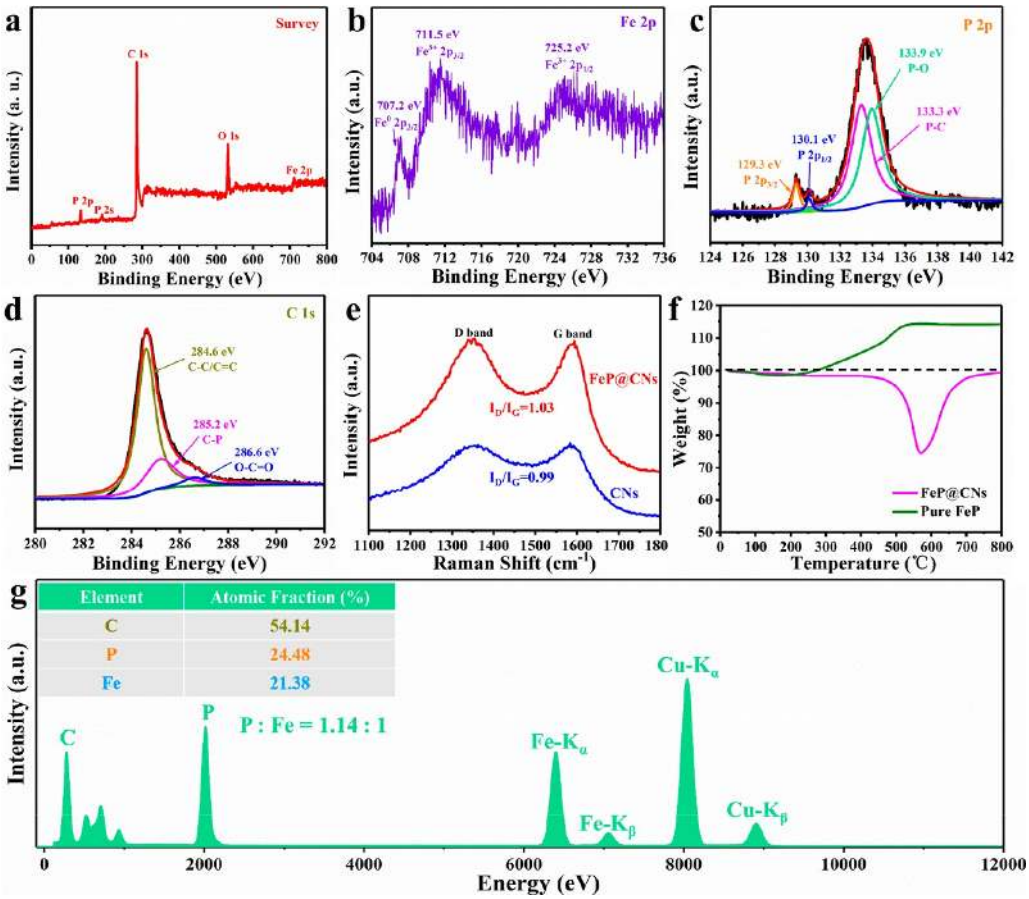

Figure 3. (a) Full-scale XPS spectrum and the high-resolution XPS spectra of (b) Fe 2p, (c) P 2p, and (d) C 1s of the FeP@CNs. (e) Raman spectra of FeP@CNs and CNs. (f) TGA profiles of FeP@CNs and pure FeP. (g) EDX spectrum of FeP@CNs and the corresponding elemental contents.

The detailed formation process of the FeP@CNs composite is schematically illustrated in Figure 2a. First, the ultrathin 3D CNs are dispersed in ferric nitrate nonahydrate solution and serve as a conductive carbon skeleton. Then the phytic acid (PA) as a phosphorus source is added dropwise to the above solution, so the PA can cross-link with the ferric ion on the CNs to generate single precursors. Subsequently, the dried precursors are annealed at 900 °C for 1 h under Ar atmosphere to obtain FeP@CNs composites with the P doping in the CNs. The morphologies and structures of the as-synthesized FeP@CNs, bare CNs, FeP-C, bare FeP, and P-doped CNs are investigated by FESEM and TEM, as shown in Figure 2 and Figures S4, S6, S7, and S8, respectively. The CNs possess 3D flower morphology with vertically aligned petals like CN (Figure S4a−c) and make up the assembly of fully interconnected 3D CNs with ultrathin walls (<10 nm) containing a few stacked graphitic layers (Figure S4d,e), forming an open and highly porous architecture (Figure S4f). This structure is highly beneficial in accommodating the volume variations of FeP during battery cycling and ensuring convenient channels for fast Li ion electron transport.[46,47] After the integration of FeP nanoparticles (average about 80 nm in size), as illustrated in Figure 2b,c, the flake 3D porous CNs framework structure is well retained and FeP nanoparticles are fully encapsulated into the flake network CNs matrix forming 3D flake-CNs-like configuration. TEM images of Figure 2d,e clearly demonstrate that the numerous FeP nanoparticles are well distributed and tightly immobilized into interconnected 3D flake CNs, consistent with SEM results. The inset selected area electron diffraction (SAED) image of Figure 2e indicates the FeP nanoparticles are amorphous, corresponding to the XRD pattern of FeP@CNs (Figure S5). High-resolution TEM (HRTEM) images further reveal the amorphous nature of FeP, which is tightly wrapped by the ultrathin CNs that are composed of a few graphitic layers. The high-angle annular dark-field (HAADF) scanning transmission electron microscopy (STEM) (Figure 2g) and elemental mapping images in Figure 2h−j present the C, P, and Fe elemental distributions, which clearly demonstrate that nanosized FeP nanoparticles are uniformly embedded into microstructural features of interconnected 3D CNs frameworks, revealing the hybrid structure of FeP@CNs integrating the features of micro- and nanostructures. For comparison, the P-doped CNs are prepared by removing the internal FeP nanoparticles of FeP@CNs composites. The morphologies and structures of CNs can be well maintained, featuring the 3D flake-network-CNs (Figure S8a−c). The HAADF and elemental mapping images clearly demonstrate that the P element is dispersed uniformly throughout the CNs (Figure S8d−f), further confirming the successful doping of P in CNs. The FeP particles coated with a thin carbon layer (FeP-C in Figure S6a−g) are also synthesized using a procedure similar to that of FeP@CNs except omitting CNs. The bare FeP nanoparticles (Figures S5 and S7) with uniform sizes around 20−30 nm in diameter are also synthesized using Fe_2O_3

https://dx.doi.org/10.1021/acsnano.9b08575
ACS Nano 2020, 14, 9545−9561

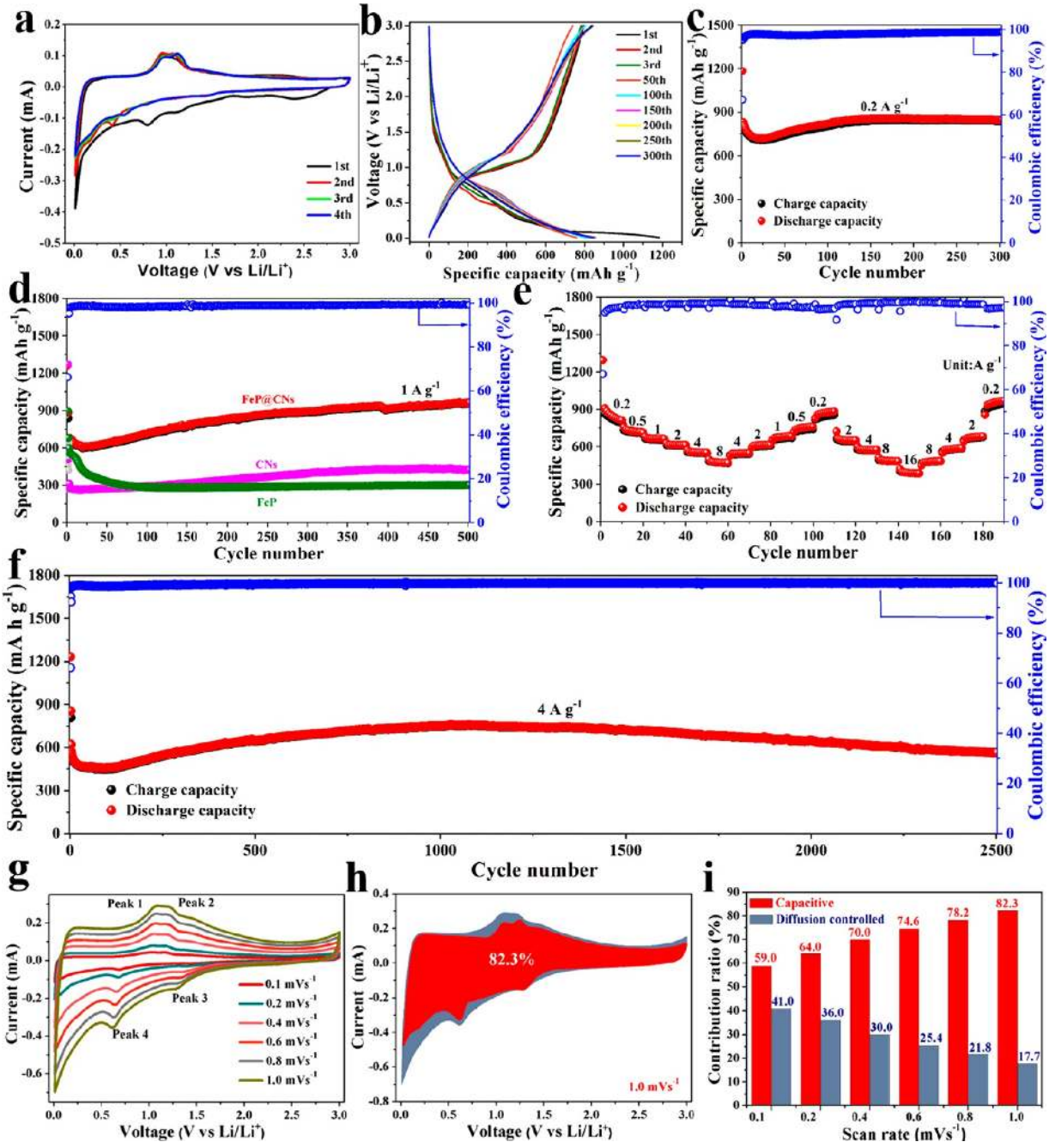

Figure 4. Electrochemical properties in half cell: (a) CV curves of the FeP@CNs electrode in the initial four cycles. (b) discharge−charge curves and (c) cycling performance of the FeP@CNs electrode at 0.2 A g^{-1}, (d) cycling performances of FeP@CNs, CNs and bare FeP electrodes at 1 A g^{-1}, (e) rate performance of FeP@CNs electrode at various current densities, (f) long-term cycling performance of FeP@CNs electrode at 4 A g^{-1}, (g) CV curves with scan rates increasing from 0.1 to 1.0 mV s^{-1}, (h) capacitive contribution (represented by the red shaded region) at a scan rate of 1.0 mV s^{-1}, and (i) the ratio of capacitive contribution at various scan rates of the FeP@CNs electrode.

nanoparticles as starting materials followed by phosphidation processes.

The chemical composition and elemental oxidation state of FeP@CNs are investigated by XPS. The XPS full spectrum in Figure 3a reveals the presence of C, O, P, and Fe on the surface of the FeP@CNs, while the P-doped CNs only show the existence of C, O, and P due to removal of the internal FeP nanoparticles (Figure S8i). The high-resolution Fe 2p XPS spectrum exhibits two apparent peaks at 711.5 and 725.2 eV, originating from Fe $2p_{3/2}$ and Fe $2p_{1/2}$ peaks, respectively.[34,52] In addition, a peak at 707.2 eV is ascribed to Fe^0 $2p_{3/2}$ from a slight reduction of Fe^{3+} during the heat treatment process, which has also been observed in the previous reports.[52,53] The high-resolution P 2p spectrum of the FeP@CNs can be deconvoluted into four peaks, as illustrated in Figure 3c. Two small peaks at 129.3 and 130.1 eV correspond to P $2p_{3/2}$ and P $2p_{1/2}$ of P in FeP, respectively.[54] The P−C (structural model shown in Figure S9c) observed at 133.3 eV can be related to a handful of P doping in CNs,[54] which is also supported by the Fourier transform infrared spectrometer (FTIR) and Raman results (Figure S9a,b). The appearance of P−O at 133.9 eV is ascribed to the oxidized phosphide on the surface of FeP@

https://dx.doi.org/10.1021/acsnano.9b08575
ACS Nano 2020, 14, 9545−9561

CNs, which is also commonly observed in reported results of TMPs.[16,31,38,52,53,55] To confirm the existence of coupling between P-doped CNs and FeP, we compare the results of high-resolution P 2p spectrum and FTIR spectra of FeP@CNs with P-doped CNs. From Figure S10a,b, it is evident that the P $2p_{3/2}$ and P $2p_{1/2}$ peaks associated with internal FeP disappear and the intensity of P−C reduces significantly, indicating that the coupling between the P in internal FeP nanoparticles with CNs has been removed and, therefore, suggesting the existence of coupling between P-doped CNs and FeP. This result is also supported by FTIR results as shown in Figure S10c. The peak at 750 cm^{-1} can be assigned to P−C stretching.[56−58] Figure S10c clearly shows that the P−C bond of P-doped CNs is weaker than the P−C bond of FeP@CNs, which further confirms the existence of coupling between P doped CNs and FeP, corresponding to the result from DFT calculation. The C 1s XPS spectrum (Figure 3d) can be fitted with three peaks located at 284.6, 285.2, and 286.6 eV, corresponding to C−C/C═C, C−P, and O−C═O, respectively.[54] To further characterize the carbon component, the Raman spectrum of the CNs, FeP@CNs, and P-doped CNs are carried out, as shown in Figure 3e and Figure S8g. It can be observed that two broad peaks centered at ∼1350 and 1590 cm^{-1}, which are assigned to the D (disordered) band and G (graphite) band of the carbon materials, demonstrate the existence of CNs.[54] The I_D/I_G ratios of FeP@CNs, CNs, and P-doped CNs are 1.03, 0.99, and 1.04, respectively. It can be seen clearly that the I_D/I_G of P-doped CNs is higher than that of CNs, indicating more defects/disorders after P doped CNs.[15,59] The content of carbon in FeP@CNs is calculated to be about 27 wt % according to the thermo-gravimetric analysis (TGA) analysis (Figure 3f) for FeP@CNs and bare FeP, together with the corresponding XRD pattern of the residue of FeP@CNs after TGA measurement (Figure S11, more details are given in Supporting Information).[34,35] The EDX spectrum of FeP@CNs in Figure 3g shows the coexistence of P and Fe, and the ratio of P to Fe is measured to be 1.14:1 according to the chart inset in Figure 3g indicating the presence of FeP. This result is in good agreement with the ratio obtained from inductively coupled plasma-atomic emission spectrometry (ICP-AES) (Supplementary Table S2). The excess P can be ascribed to the P doping in CNs, corresponding to the result of the high-resolution P 2p spectrum of XPS.

The electrochemical performance of FeP@CNs composites, bare CNs and bare FeP nanoparticles electrodes are evaluated with the standard coin-type cell configuration. The cyclic voltammogram (CV) curves of FeP@CNs electrode for four initial cycles are measured at a scan rate of 0.1 mV s^{-1} between 0.01 and 3 V. As shown in Figure 4a, the three reduction peaks at 2.42, 1.88, and 1.15 V, during the first cathodic scan, are associated with the multistep intercalation of Li^+ into the FeP to form Li_xFeP ($FeP + xLi^+ + xe^- \rightarrow Li_xFeP$ ($x = 0-3$), (A)),[34,52] and the following peak at 0.8 V corresponds to the reduction of Li_xFeP to Fe and Li_3P ($Li_xFeP + (3 - x)Li^+ + (3 - x)e^- \rightarrow Fe + Li_3P$, (B)) and the formation of solid-electrolyte interphase (SEI) film on the surface of the electrode.[34,55] During the first anodic scan, the two oxidation peaks located at 0.96 and 1.1 V are attributed to the reverse process of B, and less prominent oxidation peaks between 1.3 to 3 V are ascribed to the reverse process of A.[34,55] During the second cathodic cycle, reactions A and B mainly occur at 1.44 and 0.42 V, respectively. For the subsequent cathodic cycles, it is noteworthy that the peak of reaction B at 0.42 V is broken into two peaks at 0.42 and 0.55 V, which is mainly due to the electrochemical activation process and a certain degree of microstructure changes of FeP in the first two cycles.[30] There are no significant changes in the oxidation peaks in subsequent anodic scans. Moreover, both the cathodic and anodic peaks in the CV curves overlap from the third cycle onward, suggesting excellent reversibility and stability of the electrode. Figure 4b exhibits the charge−discharge profiles of the as-synthesized FeP@CNs electrode at a current density of 0.2 A g^{-1} in the potential range of 0.01−3 V. The discharge and charge capacities of the first cycle are 1185 and 795 mA h g^{-1}, respectively, corresponding to a first cycle Coulombic efficiency (CE) of 67.1%. The initial capacity loss is primarily due to the inevitable formation of SEI films,[60−64] which can be compensated by prelithiating the anodes through either chemical or electrochemical methods or by adding stabilized Li metal powders into the anodes.[65−67] The CE value then quickly increases to 95.4% at the second cycle and levels off at 97−99% in subsequent cycles. Figure 4c presents the cycling performance of FeP@CNs electrode at 0.2 A g^{-1}. As expected, the FeP@CNs electrode shows a stable cycling performance, retaining a high reversible capacity of 837 mA h g^{-1} after 300 cycles, suggesting outstanding cycling stability, as confirmed by the almost overlapped charge−discharge profiles in the 150th and 300th cycles (Figure 4b). The robustly structural stability upon cycling is confirmed by *ex situ* TEM analysis of the cycled electrode. As seen in Figure S12, the electrode can still retain its integrity relatively well without apparent pulverization or loss of FeP nanoparticles and the reacted FeP nanoparticles are still fully embedded in the 3D CNs framework. Figure 4d compares the cycling performance of FeP@CNs composite, bare CNs, and bare FeP electrodes at 1 A g^{-1}. Apparently, the FeP@CNs electrode outperforms the other two electrodes in cycling stability, delivering a reversible capacity of 956 mA h g^{-1} at 1 A g^{-1} without any capacity decay for 500 cycles. In contrast, the capacity of the bare FeP electrode fades rapidly, reaching 300.8 mA h g^{-1} with 46% capacity retention after 500 cycles, and a capacity of only 393 mA h g^{-1} after 500 cycles is retained for the FeP-C electrode (Figure S6h). The capacity of the CNs electrode is maintained at 418 mA h g^{-1} with 92% capacity retention after 500 cycles, while a specific capacity of 486.8 mA h g^{-1} after 500 cycles at 1 A g^{-1} can be maintained for P-doped CNs electrode, which is higher than that of bare CNs electrode (418 mA h g^{-1}) (Figure S8j). Moreover, the rate performance of P-doped CNs electrode is also better than that of bare CNs electrode (Figure S8k). The enhanced electrochemical performances of P-doped CNs electrode could be attributed to the presence of structural defects in CNs after P doping, which is beneficial for providing more active sites for Li storage as well as enhancing the kinetics of Li^+ transport during cycling.[15,68−70] The capacity decay in the initial few cycles for FeP@CNs electrode is probably ascribed to the lithiation-induced structure reorganization and the formation of unstable SEI.[71,72] The rising capacity after the initial few cycles, which is commonly observed in various nanostructured anodes,[23,73−76] is likely due to lithiation-induced structural optimization and the reversible formation of organic polymeric/gel-like layer caused by electrolyte decomposition, which can offer a large fraction of electrochemical reaction interface for storage of excess Li^+ ions through a so-called "pseudo-capacitance-type behavior".[71,77,72] This phenomenon is further confirmed by the capacity plateau changes shown in Figure S13 and kinetic analysis in Figure 4g-i.

https://dx.doi.org/10.1021/acsnano.9b08575
ACS Nano 2020, 14, 9545−9561

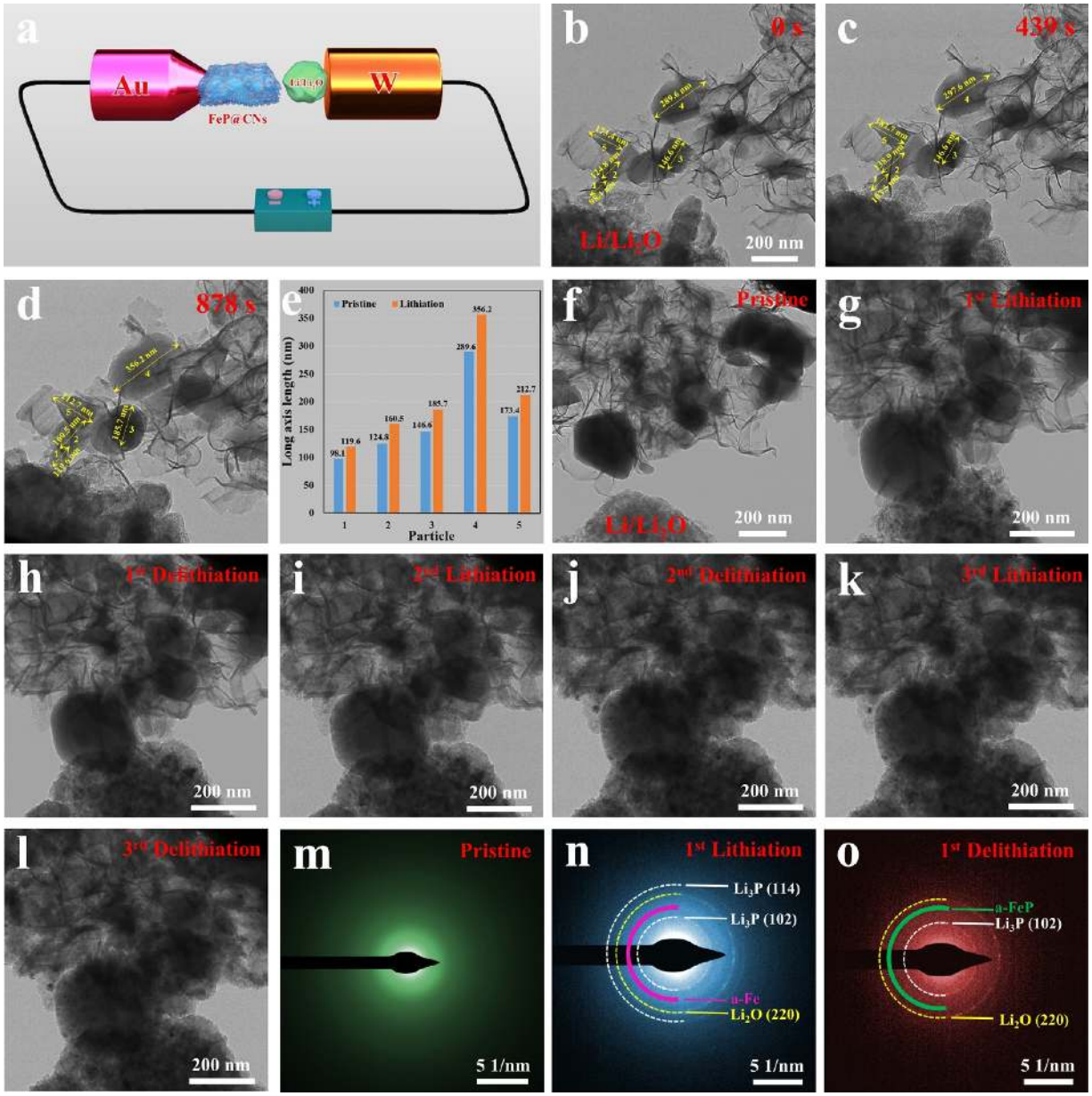

Figure 5. (a) Schematic illustration of the *in situ* TEM electrochemical cell. (b–d) Time-resolved TEM images for FeP@CNs electrode during lithiation. (e) The histogram statistics of the increase of long axis length for corresponding particles. *In situ* TEM images of (f) another pristine FeP@CNs electrode, (g) after the first lithiation, (h) after the first delithiation, (i) after the second lithiation, (j) after the second delithiation, (k) after third lithiation, and (l) after the third delithiation. The corresponding SAED patterns of (m) another pristine FeP@CNs electrode, (n) after the first lithiation, and (o) after the first delithiation.

Furthermore, the FeP@CNs electrode exhibits prominent rate capability, as illustrated in Figure 4e. It can deliver a high reversible capacity of 870, 733, 665, 614, 559, and 485 mA h g^{-1} upon increasing rates of 0.2, 0.5, 1, 2, 4, and 8 A g^{-1}, respectively. Impressively, even at large rates up to 16 A g^{-1}, a high reversible capacity of 403 mA h g^{-1} (46% of the capacity at 0.2 A g^{-1}) can be achieved, which is excessively higher than that of bare FeP nanoparticles, bare CNs, FeP-C and P-doped CNs electrodes (Figure S14, Figure S6i, and Figure S8k). When the current rate finally returns to 0.2 A g^{-1}, more than 945 mA h g^{-1} after 190 cycles at rates ranging from 0.2 to 16 A g^{-1} can still be achieved, suggesting outstanding rate tolerance and excellent structure robustness. In comparison, the bare FeP electrode exhibits a low capacity of 154.6 mA h g^{-1} at 8 A g^{-1} with only 24.6% capacity retention from 0.2 to 8 A g^{-1} (Figure S14). The improved reaction kinetics of the FeP@CNs electrode is confirmed by electrochemical impedance spectra (EIS) results (Figure S15a), where the FeP@CNs electrode shows much lower charge-transfer resistance both before and after cycling, indicative of faster charge transfer and higher electrode conductivity than the bare FeP. The apparent difference in capacity retention at high rates emphasizes the vital role of the 3D flake-CNs-like structure in enabling the ultrafast rate capability of the FeP@CNs electrodes, which is also evidenced by CV results in Figure 4g–i. In addition to its outstanding rate capability, FeP@CNs electrode also exhibits extraordinary long-term cycling stability, retaining a specific capacity of 563 mA h g^{-1} with 98% capacity retention over 2500 cycles at a high cycling current density of 4 A g^{-1}, demonstrating the excellent structural stability upon cycling.

https://dx.doi.org/10.1021/acsnano.9b08575
ACS Nano 2020, 14, 9545–9561

From the *ex situ* TEM images shown in Figure S16a–d, the electrode structure of the FeP@CNs after long-term cycling is well preserved without visible structural collapse while the reacted FeP nanoparticles are still tightly immobilized in the CNs scaffold, suggesting that the CNs is robust enough to buffer the volume variation of FeP nanoparticles and thus contribute to excellent structural stability. According to the elemental mapping results in Figure S16e–l, the features of FeP nanoparticles embedded into a microsized CNs frame can be clearly identified, confirming that the hybrid structure of the FeP@CNs is retained. Further evidence for the robust structural stability of FeP@CNs electrode after long-term cycling can be confirmed by EIS analysis (Figure S15b). These results clearly indicate that the FeP@CNs electrodes demonstrate superior performance in terms of large capacity, high rate capability, and long cycle stability outperforming the large majority of TMPs-based anodes (Supplementary Table S3) as well as TMO- and TMS-based anodes in previously reported works (Supplementary Table S4). Encouragingly, the FeP@CNs electrodes also present outstanding Na storage performance in terms of high reversible capacity, superior rate performance, and an extremely stable cycling life (Figure S17), further confirming the advantageous structural features of FeP@CNs for electrochemical energy storage.

To elucidate the reason for the high-rate capability of the FeP@CNs electrode, its electrochemical reaction kinetics are further investigated using cyclic voltammetry (CV) at different scan rates from 0.1 to 1 mV s^{-1}. From Figure 4g, it is evidently observed that all of the CV curves display similar shapes and nearly the same anodic/cathodic peak separation when the scan rate is increased from 0.1 to 1.0 mV s^{-1}, suggesting small polarization and fast kinetics of the FeP@CNs electrode. In general, the voltammetric response of an electrode-active material at various sweep rates can be qualitatively measured by the relationship between the peak current (i) and scan rate (v) from CV curves according to

$$i = av^b \tag{1}$$

$$i = k_1 v + k_2 v^{1/2} \tag{2}$$

where a and b and k_1 and k_2 are adjustable parameters and constant parameters, respectively.[30,78,79,80] The b value can be calculated by plotting $\log(i)$ versus $\log(v)$. Generally, a constant b value approaching 0.5 or 1 indicates a diffusion-controlled or capacitance-controlled process, respectively.[62,79] By plotting the linear relationship between $\log(i)$ and $\log(v)$, the calculated b values (Figure S18) determined by the anodic (peak 1 and peak 2) and cathodic (peak 3 and peak 4) slopes are 0.83, 0.83, 1.00 and 0.87, respectively, suggesting a hybrid Li storage mechanism that is dominated by a capacitance-controlled process. By distinguishing the current (i) from the diffusion and capacitance according to eq 2, the ratios of capacitive contribution are further determined quantitatively. Clearly, at the scan rate of 1.0 mV s^{-1}, a significantly high capacitive contribution of 82.3% is obtained for FeP@CNs electrode, indicating a fast capacitive-dominant characteristic. Upon increasing the scan rate from 0.1 to 1.0 mV s^{-1}, the capacitive contribution of the FeP@CNs electrode increases from 59.0 to 82.3%, demonstrating a fast-growing pseudocapacitive effect with an increasing rate, which is highly beneficial for enhancing the rate capability. The significant enhancement of capacitive behavior can be mainly derived from the collective effects from the structural superiority of FeP@CNs, in which nanosized FeP affords reduced paths for both ion and electron diffusion while the 3D porous CNs provides a highly efficient electrochemical circuit around the FeP nanoparticles and endows large electrode/electrolyte interfaces for high ion flux across on the surfaces and/or interfaces, accounting for high-rate lithium storage capability.[16,81]

To further uncover the structural and phase evolution of the FeP@CNs composite electrode during the lithiation/delithiation process, *in situ* TEM through a nanobattery configuration, as schematically shown in Figure 5a, has been employed in real time.[51,82] Figure 5b–d shows the time-lapse TEM images of the morphological evolution of FeP@CNs electrode during lithiation (captured from supplementary *in situ* movie 1). In the initial state (Figure 5b), it is evidently observed that that the FeP nanoparticles are fully confined into ultrathin 3D interconnected CNs. Upon reaction, a potential of −6 V is applied to the FeP@CNs to initiate the lithiation. As shown in Figure 5c, three neighboring FeP nanoparticles (particle 1, 2, and 5) present notable volume expansion after lithiation for 439 s; the long axis of particles 1, 2, and 5 increases from about 98.1 to 103.5 nm, 124.8 to 138.9 nm, and 173.4 to 182.7 nm, respectively. Meanwhile, the nearby ultrathin CNs also clearly thicken, indicating the lithiation process of CNs, contributing part of the capacity to FeP@CNs composite. As the lithium diffusion continues, the lithiation of the farther FeP particles (particles 3 and 4) and CNs occurs. After 878 s of lithiation, the increase of long axis length of corresponding particles is shown in histogram statistics (Figure 5e) and is estimated to be 21.9%, 28.6%, 26.6%, 23.0%, and 22.7%, respectively. The time-lapse enlarged TEM images (Figure S19) (captured from supplementary *in situ* movie 2) of another FeP@CNs composite demonstrate more clearly the size variations of amorphous FeP nanoparticles during the lithiation process. Interestingly, during the whole lithiation process, the FeP@CNs composite maintains its original morphology without observing any structural degradation such as structural collapse or cracks internal FeP nanoparticles, suggesting that the CNs matrix and the porous structure can effectively buffer the volume expansion and prevent the pulverization of the FeP nanoparticles during lithiation. More impressively, even after almost 30 min of lithiation, the original morphology of FeP@CNs is still well-maintained without any cracks (Figure S20, captured from supplementary *in situ* movie 3). Robust structural stability of the FeP@CNs electrode is further characterized after repeated lithiation/delithiation cycles by applying a constant bias (−6/6 V) as presented in Figure 5f–l (captured from supplementary *in situ* movie 4). Before lithiation, the FeP@CNs has no noticeable FeP diffraction patterns due to the amorphous nature of the sample (Figure 5m). After the first lithiation, although the internal FeP nanoparticles experience noticeable volume changes, no cracks are observed (Figure 5g). The corresponding SAED pattern in Figure 5n presents the emergence of diffraction rings from Li_3P (JCPDS no. 04-0525) and diffusion halos of amorphous Fe, revealing the conversion reaction process of the FeP@CNs electrode after the first lithiation. The existence of diffraction rings of Li_2O is likely due to the slight oxidation of Li in the TEM environment.[83] Reversely, after the first delithiation, the internal FeP nanoparticles have almost no observable structural change except for size reduction. Meanwhile, the corresponding SAED image shows the Li_3P (114) diffraction ring has almost disappeared, the diffraction ring of Li_3P (102) is also inconspicuous and the diffusion halos of amorphous FeP grow

https://dx.doi.org/10.1021/acsnano.9b08575
ACS Nano 2020, 14, 9545–9561

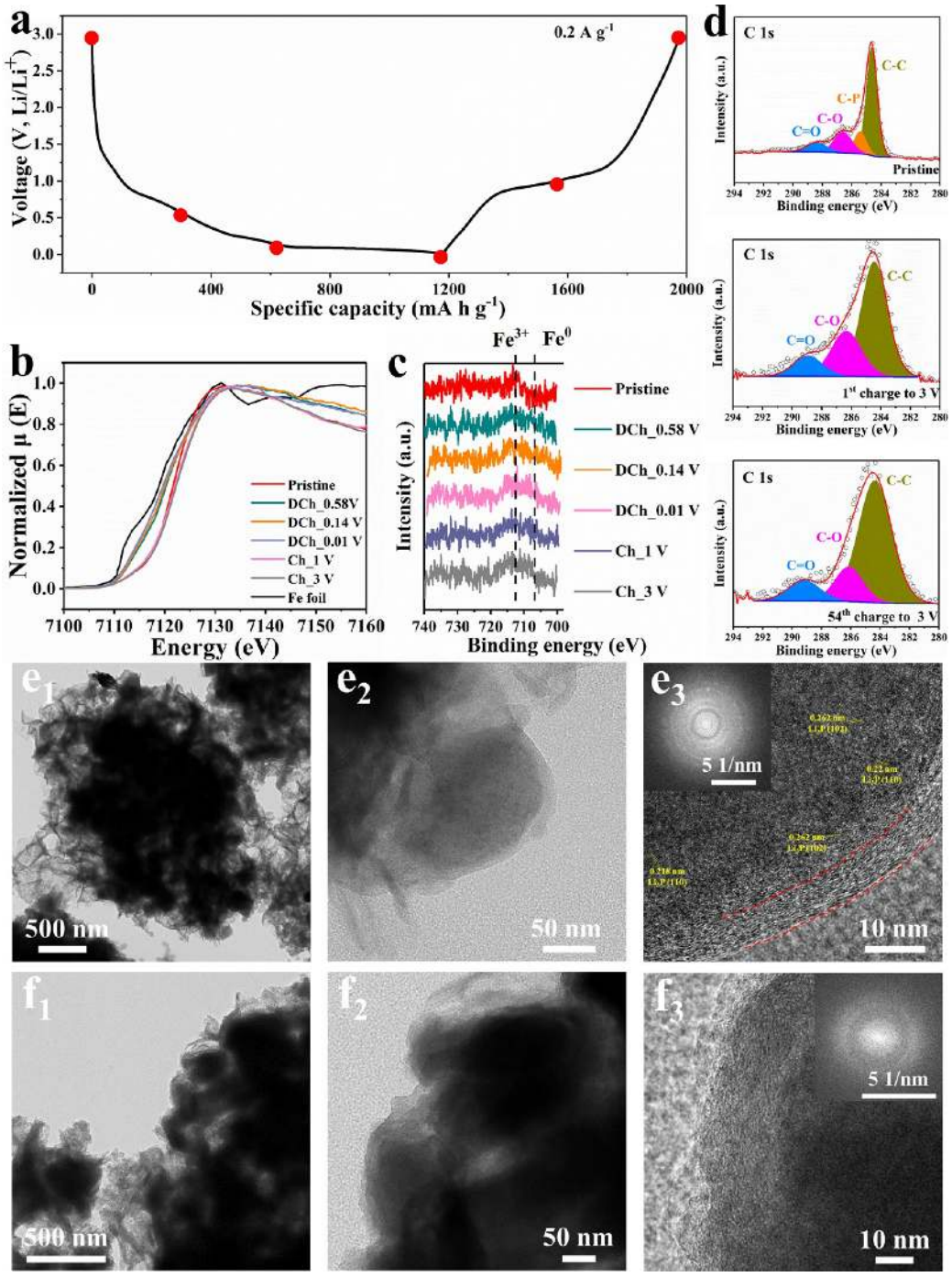

Figure 6. (a) First cycle voltage profile of FeP@CNs at 0.2 A g^{-1}. (b) *Ex situ* XAS of Fe K-edge at different states of (dis)charge. (c) *Ex situ* XPS of Fe 2p region at different states of (dis)charge. (d) *Ex situ* XPS of C 1s region at delithiated state in different cycles. TEM, HRTEM, and corresponding FFT images of FeP@CNs electrodes at different states: (e1−e3) first discharge and (f1−f3) first charge.

in the SAED after the first delithiation, indicating the regeneration of FeP nanoparticles (Figure 5o). These results are thereafter ascertained with *ex situ* X-ray absorption near-edge structure (XANES) spectra, X-ray photoelectron energy spectra (XPS) and TEM observations of cycled samples in Figure 6. Noticeably, the diffraction ring of Li_3P (102) that is still detected but diminishes in the delithiated electrode is probably due to the difficulty of full conversion with an *in situ* TEM setup.[84] Impressively, this lithiation/delithiation cycling (Figure 5h−k) of the FeP@CNs can be repeated with similar rates for several times without observing any unstable structural changes such as cracking and fracture, indicating the high structure integrity, correlating well with the *ex situ* TEM results. It worth mentioning that the surface fluctuations occurs after a few cycles, which are caused by the growth of Li_2O on the FeP@CNs surface.[85] From all of the observations above, we see the stable structural change of FeP@CNs during multiple lithiation/delithiation cycling, contributing to the excellent cycling performance of this anode material.

The charge compensation mechanism of FeP@CNs in its first cycle is investigated by XANES spectra and XPS. The Fe K-edge (7132 eV) of pristine and cycled FeP@CNs electrodes

https://dx.doi.org/10.1021/acsnano.9b08575
ACS Nano 2020, 14, 9545−9561

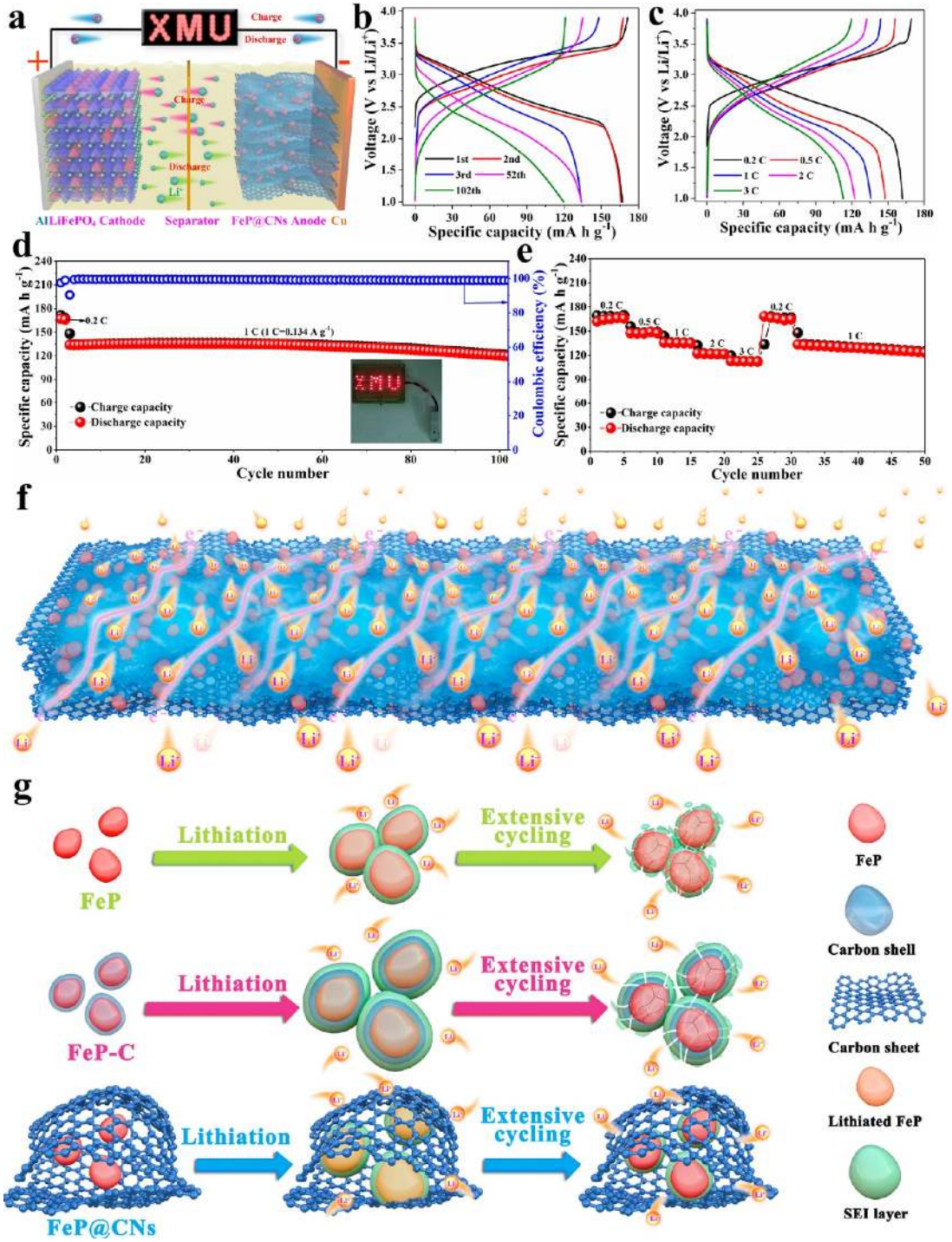

Figure 7. (a) Schematic illustration of the full cell, (b) charge−discharge curves at 1C, (c) charge−discharge curves at various C rate, (d) the cycle performance of $LiFePO_4$//FeP@CNs full-cell at 1 C, the inset digital photo is a XMU logo consisting of 32 red LEDs in parallel powered by the full cell, (e) the rate performance of $LiFePO_4$//FeP@CNs full cell at various C rate from 0.2 to 3 C, (f) schematic illustration of the rational design of the FeP@CNs anode for LIBs and (g) schematic illustration of the morphology evolutions of bare FeP nanoparticles, FeP-C and FeP@CNs electrodes. The 3D flake-CNs-like architecture of FeP@CNs is effective in accommodating the volume change of active FeP without pulverization, while the bare FeP nanoparticles and FeP-C electrodes are prone to pulverize during repeated cycling, leaving cracks on both active FeP and SEI layer.

is shown in Figure 6b. When the FeP@CNs is discharged to 0.01 V, the Fe K-edge spectrum shows a clear shift toward the lower energy region compared with the as-prepared state. The shoulder of the FeP@CNs at 0.01 V is slightly higher than the Fe foil. This indicates that the reduction of Fe ions mainly compensates for the electron harvest at this step. When the material is charged back to 3.0 V, the shift to the higher energy region in the Fe K-edge is clearly seen. After one cycle, the Fe K-edge recovers to its original state, suggesting the reaction is highly reversible. This is consistent with the observed *in situ* TEM result; the majority of Fe^{3+} is reduced to Fe^0 after FeP@CNs is discharged to 0.01 V, leading to the formation of

https://dx.doi.org/10.1021/acsnano.9b08575
ACS Nano 2020, 14, 9545−9561

elemental Fe.[86,87] Figure 6c presents the *ex situ* XPS results of Fe 2p region. The binding energy peaks at ~712 and ~707 eV correspond to Fe^{3+} and Fe^0, respectively. At the pristine state, the surface of FeP@CNs is dominated by Fe^{3+}. During the discharge, the Fe^0 starts to appear and becomes the main species at 0.01 V. After one cycle, the Fe^{3+} dominates the surface as a result of electron loss during the charge. Both XAS and XPS verify that the Fe^{3+}/Fe^0 is the main active redox couple during cycling. The irreversible capacity in the first cycle of FeP@CNs is due to the formation of SEI, which has been observed by TEM (Figure 6e,f). The XPS of C 1s region (Figure 6d) of the cycled FeP@CNs exhibits significant C−O and C═O features at ~286 and ~289 eV due to the decomposition of carbonate solvent. Both peaks do not show obvious change from the first cycle to the 54th cycle, implying the SEI is stable once it is formed in the initial cycle. It should be noted that the absence of the C−P peak in the cycled FeP@CNs may originate from the coverage of the material by the SEI, which buries the signal of the P doped CNs. The stable SEI and highly reversible Fe^{3+}/Fe^0 redox contribute to the excellent cycling stability of the FeP@CNs. Parts e and f of Figure 6 show the *ex situ* TEM images of the FeP@CNs electrode after initial discharge and charge states. As illustrated in Figure 6e1−e2, the electroactive particles are coated by the thickened CNs, well maintaining the 3D network-like structure after initial discharge. HRTEM and FFT images (Figure 6e3) show the reacted FeP consisting of many polycrystalline nanograins, which are related to the formation of Li_3P after first lithiation. This is consistent with the SAED result of *in situ* TEM observation. Parts f1 and f2 of Figure 6 show the morphology of the electrode similar to that of the first discharge process without any unstable structural changes after the initial charge. The HRTEM image and the corresponding FFT image reveal the regeneration of amorphous electroactive particles (Figure 6f3).

To demonstrate the practical application of FeP@CNs as an anode material for LIBs, the full cell using $LiFePO_4$ as a cathode and prelithiated FeP@CNs as an anode is assembled, as illustrated in Figure 7a. The charge−discharge profiles of $LiFePO_4$ cathode and prelithiated FeP@CNs anode in a half cell are given in Figure S21. The typical charge−discharge profiles of the full cell at a current density of 1 C with a voltage window of 1.0−3.9 V are shown in Figure 7b. The initial charge and discharge capacity are 171.4 and 167.0 mA h g^{-1} at 0.2 C (1C = 170 mA h g^{-1}, based on active material in cathode), respectively, displaying a high initial CE of 97.4%. Figure 7d depicts the corresponding cycle performance of the full cell at a current density of 1 C (activated at 0.2 C for two cycles). The as-obtained full-cell exhibits a high reversible capacity of 119.6 mA h g^{-1} with a capacity retention of 89.3% for over 100 cycles at 1 C. The inserted photo image in Figure 7d shows how this full battery can power a 32 red LED array with XMU (Xiamen University) logo, highlighting the enormous potential of our FeP@CNs anodes for practical applications. Figure 7c shows the charge−discharge curves of the full cell at various current densities from 0.2 to 3 C. Impressively, it can achieve reversible capacities of 169.1, 147.5, 135.7, 122.3, and 112.8 mA h g^{-1} at 0.2, 0.5, 1.0, 2.0, and 3.0 C, respectively, with a capacity retention of 66.7% from 0.2 to 3 C. When the current density returns to 0.2 C, a reversible capacity of 166.5 mA h g^{-1} after 5 cycles can be recovered (98.5% of the initial capacity), by another 20 repeated cycles at 1 C which displays the capacity of 123.4 mA h g^{-1} (Figure 7e), implying the excellent tolerance for the rapid Li insertion/extraction reactions.

The superior electrochemical performance of the FeP@CNs electrode can be attributed to the compositional and structural benefits of the composite, which offers multiple advantages for high performance. First, the P doped on CNs and the existence of coupling between FeP- and P-doped CNs not only enable the hybrid with improved electronic conductivity and more charge storage sites but also promote the reversibility of conversion reaction, as revealed by DFT calculations, favoring improved capacity and rate performance. Second, as schematically demonstrated in Figure 7f, the 3D-interconnected CNs confine the FeP nanoparticles and function as an elastic buffer to prevent pulverization/aggregation of encapsulated FeP nanoparticles during cycling (Figure 7g) maintain the active surface and leave stable and unobstructed channels for the fast electron (high conductivity) and Li-ion (short diffusion length) transport.[33,46] This gives rise to outstanding rate capacity and stable cycling performance. Meanwhile, the 3D porous structure of CNs not only enables full utilization of active FeP nanoparticles and abundant accessibility of electrolyte but also offers a structure-buffering space to accommodate the mechanical stress from the volume variation of embedded FeP nanoparticles during repeated cycling without destroying the structural and electrical integrity of electrodes as shown in Figure 7g,[46,47] contributing to high capacity and excellent long-term cycling stability, which is confirmed by *in situ* and *ex situ* TEM measurements. Additionally, the amorphous structure of active FeP is highly beneficial in reducing the risk of fracture during cycling[16,42] and nanoscale FeP shortens the electron/ion transport path,[16] leading to enhanced cycling stability and reaction kinetics.

CONCLUSIONS

In summary, DFT calculations have predicted the existence of coupling between FeP- and P-doped CNs, and the doping of P on CNs not only enables the hybrids with improved conductivity and abundant active sites for charge storage but also promotes the reversibility of discharge product (Li_3P) *via* reducing its dissociation energies, implying enhanced capacity and rate performance. In light of these theoretical analyses, an excellent LIBs anode candidate of 3D flake-CNs-like configuration, consisting of amorphous FeP nanoparticles encapsulated into ultrathin 3D interconnected P-doped porous CNs, has been successfully developed *via* delicate architecture design and facile synthesis approach. By virtue of the structural characteristics and compositional features, the FeP@CNs anode exhibits a high reversible capacity of 837 mA h g^{-1} after 300 cycles at 0.2 A g^{-1} and superb rate capability of 403 mA h g^{-1} at 16 A g^{-1}, while maintaining extraordinary cycling stability even up to 2500 cycles with a capacity retention of 98% at 4 A g^{-1}. Impressively, the anode also demonstrates the superior sodium-ion storage properties, namely, outstanding rate capability and long-life cycling stability. The full cell-based on prelithiated FeP@CNs anode exhibits a high reversible capacity of 119.6 mA h g^{-1} at 1 C with a capacity retention of 89.3% over 100 cycles as well as impressive rate capability. A combined *ex situ* XANES, XPS, and TEM analysis proves the high reversibility of conversion reaction and excellent structural integrity during cycling, accounting for superior performance. Further *in situ* TEM measurements show strong evidence that the 3D flake-CNs-like structure with amorphous FeP nanoparticles confined in CNs plays a crucial role in

https://dx.doi.org/10.1021/acsnano.9b08575
ACS Nano 2020, 14, 9545−9561

accommodating the volume change and preventing pulverization/aggregation of FeP during cycling, contributing to long-term stabilization. Our findings in this work are expected to provide critical scientific insights in the development of high-performance and durable anodes for advanced LIBs together with other battery chemistries.

METHODS

DFT Calculations. The DFT calculations are performed by the Quantum-ESPRESSO suite of codes.[88,89] An energy cutoff of 40 Ry is employed, while both the atomic positions and lattice parameters of pristine CN are allowed to fully relax until the Hellmann−Feynman forces on each atom became lower than 10^{-2} eV $Å^{-1}$. The pristine CN, bare FeP particle, and FeP particle on the P-doped CN (also denoted as FeP@CN) are modeled by the supercell of carbon nanosheet 3 × 3× 1 grids for the k-point sampling. The spin-polarized generalized gradient approximation (GGA) in the form of Perdew−Burke−Ernzerhof (PBE) functional and DFT-D3 correction is employed for the atomic optimization and energy calculation.[90] The adsorption energy (E_{ad}) of a single Li atom on the substrate (CN, FeP, and FeP@CN) is obtained according to eq 2,

$$E_{ad} = E_{Li+substrate} - E_{substrate} - \mu_{Li} \quad (3)$$

where $E_{Li+substrate}$, $E_{substrate}$, and μ_{Li} are the total energies of the substrate with and without considering a single Li atom adsorption and the energy of Li obtained from the bcc metal phase. The electron transfer between the Li atom and substrate is calculated by

$$\Delta\rho = \rho_{Li+substrate} - \rho_{substrate} - \rho_{Li} \quad (4)$$

where $\rho_{Li+substrate}$, $\rho_{substrate}$, and ρ_{Li} are the electron densities of Li adsorbed structure, substrate, and the isolated adsorbed Li atom, respectively.

Periodic boundary conditions are adopted for the simulation cell and a vacuum layer of at least 15 Å is added along the out-of-plane direction to eliminate the interactions between adjacent sheet images. The charge transfer mechanism is studied by employing Bader charge analysis. To analyze the energy barrier of the Li diffusion on FeP surface and the dissociation from $Li_3P \rightarrow Li_2P + Li$, at least six transitional images are used in the climbing image NEB (CI-NEB) calculation.

Synthesis of Ultrathin 3D Carbon Nanosheets. The ultrathin three-dimensional carbon nanosheets are prepared as follows: 5 g of sodium dihydrogen citrate is first annealed at 780 °C for 2 h with a heating speed of 5 °C min^{-1} under an argon atmosphere. After cooling to room temperature naturally, the black solid product is washed with 2 M HCl solution for 24 h to remove sodium compounds thoroughly. Then the final product of the porous CNs is collected by filtration, rinsed with distilled water and ethanol several times, and dried at 70 °C for 2 h.

Synthesis of Amorphous FeP@CNs Composites and P-Doped CNs. In a typical synthesis, 0.36 g of $Fe(NO_3)_3{\cdot}9H_2O$ is dissolved in a mixed solution of 10 mL of deionized water and 10 mL of ethanol under stirring for 10 min. Then 30 mg of porous CNs is added in the above solution with 30 min ultrasonication and 10 min stirring to form a homogeneous suspension. Subsequently, 2 mL of phytic acid (PA) is added dropwise. After another 30 min of ultrasonication and 10 min of stirring, the well-dispersed black suspension is dried at 70 °C overnight, and the final solid mixture is annealed at 900 °C for 1 h under an Ar atmosphere. After that, the black products are obtained, washed by filtration with deionized water three times to remove the residue of reactants, and finally dried at 80 °C under vacuum for overnight (>12 h). The P-doped CNs are prepared by using 2 M hydrochloric acid (HCl) for 24 h to remove the internal FeP nanoparticles of the FeP@CNs composites.

Synthesis of Bare FeP Nanoparticles. $Fe(CH_3COO)_2$ (1 mM) is dissolved thoroughly in 30 mL of deionized water by stirring for 10 min. Then the solution is transferred into a Teflon-lined autoclave and kept at 180 °C for 12 h. After cooling to room temperature, the Fe_2O_3 nanoparticles are obtained by washing and drying treatment. Subsequently, the Fe_2O_3 and NaH_2PO_2 with a weight ratio of 1:30 are placed in two separate positions of the tube furnace, with NaH_2PO_2 at the upstream of a quartz tube. The samples are then heated under 500 °C for 3 h with a heating rate of 2 °C min^{-1} in the Ar atmosphere. The FeP nanoparticles are obtained after naturally cooling to room temperature.

Material Characterization. The morphology and microstructure of the as-prepared samples are characterized by field-emission scanning electron microscopy (FESEM, Hitachi SU-70) and transmission electron microscopy (TEM, FEI, Talos-F200, 200 kV). The crystal structure and chemical compositions of the products are performed by X-ray diffraction (XRD, PANalytical X'pert PRO X-ray diffractometer, Cu Kα radiation, 40 kV, 40 mA) and X-ray photoelectron energy spectra (XPS, Kratos Axis Ultra-DLD system, Shimadzu Co., Ltd., Hong Kong). Raman spectroscopy is carried out on a HORIBA LabRAM HR Evolution Raman spectrometer using an argon ion laser with a wavelength of 532 nm. Thermogravimetric (TG) analysis is implemented from room temperature to 800 °C with a heating rate of 10 °C min^{-1} by using an SDT-Q600 thermal analyzer in an air atmosphere. The *ex situ* Fe K-edge XAS spectra are measured at beamline 5.3.1 at the Advanced Light Source (ALS), Lawrence Berkeley National Laboratory (LBNL). The X-ray beam size is ∼100 μm × 100 μm. The XAS spectra are collected in total fluorescence yield mode. All the XAS spectra are measured under constant helium flow in the sample chamber.

Electrochemical Characterization. The electrochemical performances are evaluated in CR2025 half cells and full cells which are assembled in a glovebox in an argon atmosphere. The working electrodes are prepared by coating the slurry of the above active materials (FeP@CNs, bare FeP, and CNs), Super P, and sodium carboxymethyl cellulose (CMC) with a mass ratio of 80:10:10 using deionized water as the solvent on Cu foil. The electrodes are dried at 80 °C under vacuum overnight before pressing and cutting into disks. The loading of the FeP@CNs is about 1.0−1.2 mg cm^{-2} on each of the disks. The capacity of FeP@CNs is calculated based on the whole mass of FeP@CNs. Li foil is used as the counter electrode, Celgard 2400 film serves as the separator, and the electrolyte contains 1 M $LiPF_6$ dissolved in a mixture of ethylene carbonate (EC), diethyl carbonate (DEC), and dimethyl carbonate (DMC) (1:1:1 by volume). The electrochemical measurements are carried out on a Neware battery tester in a voltage window from 0.01 to 3.0 V. Cyclic voltammetry (CV) and electrochemical impedance spectroscopy (EIS) tests are conducted on a CHI 660E electrochemical workstation (Chenhua, Shanghai). The full cells are assembled with prelithiated FeP@CNs as the anode and $LiFePO_4$ (LFP) as the cathode. The prelithiation process for FeP@CNs anode is conducted using half cells by discharging to 0.01 V at 0.2 A g^{-1}, considering the low initial CE of about 67%. The cathode electrode is fabricated by mixing LFP (80 wt %), Super P (10 wt %) and polyvinylidene fluoride (PVDF, 10 wt %) is dissolved in *N*-methyl-2-pyrrolidone (NMP) to form a slurry and spread onto Al foil. To balance the capacity between cathode and anode, the cathode/anode ratio is controlled at about 1:1.2 to ensure the optimized performance of the as-prepared full cell. The $LiFePO_4$//FeP@CNs full cells are galvanostatic charged/discharged between 1.0 and 3.9 V. The capacity of the full cell is calculated on the basis of the mass of active material in the cathode.

As for sodium-ion batteries, sodium foils prepared from bulk sodium (Aladdin) serve as the counter/reference electrode and the glass fiber (Whatman) acts as the separator. The electrolyte is 1 M $NaClO_4$ in a mixture of ethylene carbonate (EC) and dimethyl carbonate (DEC) (1:1 by volume). The working electrode preparation process is the same as that in the LIB described above.

***In Situ* TEM Observation.** The *in situ* nanoscale electrochemical experiments are conducted by using the Nanofactory TEM holder operated at 200 kV. The FeP@CNs sample and a piece of Li metal are attached on and mounted to the individual side of the holder with Au and W rods, respectively. Then the sample holder is quickly transferred into TEM (FEI, Talos-F200), during which a thin native layer of Li_2O is formed due to the exposure to air. The formation of a

https://dx.doi.org/10.1021/acsnano.9b08575
ACS Nano 2020, 14, 9545−9561

Li_2O layer can serve as a solid electrolyte allowing Li^+ ion transport. Lithiation of FeP@CNs took place after a negative bias is applied to the W rod, and the delithiation starts when the bias is reversed to positive.

ASSOCIATED CONTENT

Supporting Information

The Supporting Information is available free of charge at https://pubs.acs.org/doi/10.1021/acsnano.9b08575.

First-principles calculation results of the theoretical design of advanced LIB anodes (Figures S1−S3). Experimental SEM, TEM images, BET nitrogen adsorption−desorption isotherms, XRD patterns, EDS mapping, HRTEM image, FFT image, Raman spectra, HAADF image, XPS spectra and electrochemical performance for various samples (Figures S4−S21). DFT calculation results of the adsorption, elemental composition, and the summary of the lithium storage performance of our results and other advanced anode materials (Table S1−S4) (PDF)

In situ TEM video 1 (MP4)

In situ TEM video 2 (MP4)

In situ TEM video 3 (MP4)

In situ TEM video 4 (MP4)

AUTHOR INFORMATION

Corresponding Authors

Qiaobao Zhang − *Department of Materials Science and Engineering, College of Materials, Xiamen University, Xiamen, Fujian 361005, China;* orcid.org/0000-0002-3584-5201; Email: zhangqiaobao@xmu.edu.cn

Ming-Sheng Wang − *Department of Materials Science and Engineering, College of Materials, Xiamen University, Xiamen, Fujian 361005, China;* orcid.org/0000-0003-3754-2850; Email: mswang@xmu.edu.cn

Authors

Zhiming Zheng − *Department of Materials Science and Engineering, College of Materials, Xiamen University, Xiamen, Fujian 361005, China*

Hong-Hui Wu − *Beijing Advanced Innovation Center for Materials Genome Engineering, State Key Laboratory for Advanced Metals and Materials, University of Science and Technology Beijing, Beijing 100083, China;* orcid.org/0000-0002-1381-2281

Haodong Liu − *Department of Nanoengineering, University of California San Diego, La Jolla, California 92093, United States*

Xin He − *Energy Storage and Distributed Resources Division, Lawrence Berkeley National Laboratory, Berkeley, California 94720, United States*

Sicen Yu − *Department of Nanoengineering, University of California San Diego, La Jolla, California 92093, United States*

Victoria Petrova − *Department of Nanoengineering, University of California San Diego, La Jolla, California 92093, United States*

Jun Feng − *Advanced Light Source Division, Lawrence Berkeley National Laboratory, Berkeley, California 94720, United States; Department of Materials Science & Engineering, Southern University of Science and Technology (SUSTech), Shenzhen 518055, P. R. China*

Robert Kostecki − *Energy Storage and Distributed Resources Division, Lawrence Berkeley National Laboratory, Berkeley, California 94720, United States*

Ping Liu − *Department of Nanoengineering, University of California San Diego, La Jolla, California 92093, United States;* orcid.org/0000-0002-1488-1668

Dong-Liang Peng − *Department of Materials Science and Engineering, College of Materials, Xiamen University, Xiamen, Fujian 361005, China;* orcid.org/0000-0003-4155-4766

Meilin Liu − *School of Materials Science and Engineering, Georgia Institute of Technology, Atlanta, Georgia 30332, United States;* orcid.org/0000-0002-6188-2372

Complete contact information is available at: https://pubs.acs.org/10.1021/acsnano.9b08575

Author Contributions

▽Z.Z. and H.-H.W. contributed equally to this work.

Notes

The authors declare no competing financial interest.

ACKNOWLEDGMENTS

This work is supported by the National Natural Science Foundation of China (Grant Nos. 21703185, 51872098, 21805278, and 51901013), the Leading Project Foundation of Science Department of Fujian Province (Grant No. 2018H0034), University of Science and Technology Beijing: 06500135), and the "Double-First Class" Foundation of Materials and Intelligent Manufacturing Discipline of Xiamen University. H.H.W. also acknowledges the financial support from the Opening Project of National Joint Engineering Research Center for Abrasion Control and Molding of Metal Materials, Henan University of Science and Technology (No. HKDNM201906).

REFERENCES

(1) He, T.; Feng, J.; Ru, J.; Feng, Y.; Lian, R.; Yang, J. Constructing Heterointerface of Metal Atomic Layer and Amorphous Anode Material for High-Capacity and Fast Lithium Storage. *ACS Nano* **2019**, *13*, 830−838.

(2) Zhang, Y.; Mu, Z.; Lai, J.; Chao, Y.; Yang, Y.; Zhou, P.; Li, Y.; Yang, W.; Xia, Z.; Guo, S. MXene/Si@SiO_x@C Layer-By-Layer Superstructure with Autoadjustable Function for Superior Stable Lithium Storage. *ACS Nano* **2019**, *13*, 2167−2175.

(3) Cuan, J.; Zhou, Y.; Zhang, J.; Zhou, T.; Liang, G.; Li, S.; Yu, X.; Pang, W. K.; Guo, Z. Multiple Anionic Transition-Metal Oxycarbide for Better Lithium Storage and Facilitated Multielectron Reactions. *ACS Nano* **2019**, *13*, 11665−11675.

(4) Xu, Q.; Sun, J. K.; Yu, Z. L.; Yin, Y. X.; Xin, S.; Yu, S. H.; Guo, Y. G. SiO_x Encapsulated in Graphene Bubble Film: An Ultrastable Li-Ion Battery Anode. *Adv. Mater.* **2018**, *30*, 1707430.

(5) Wu, L.; Zheng, J.; Wang, L.; Xiong, X.; Shao, Y.; Wang, G.; Wang, J. H.; Zhong, S.; Wu, M. PPy-Encapsulated SnS_2 Nanosheets Stabilized by Defects on a TiO_2 Support as a Durable Anode Material for Lithium-Ion Batteries. *Angew. Chem., Int. Ed.* **2019**, *58*, 811−815.

(6) Liu, Z.; Yu, Q.; Zhao, Y.; He, R.; Xu, M.; Feng, S.; Li, S.; Zhou, L.; Mai, L. Silicon Oxides: A Promising Family of Anode Materials for Lithium-Ion Batteries. *Chem. Soc. Rev.* **2019**, *48*, 285−309.

(7) Leng, J.; Wang, Z.; Wang, J.; Wu, H. H.; Yan, G.; Li, X.; Guo, H.; Liu, Y.; Zhang, Q.; Guo, Z. Advances in Nanostructures Fabricated *via* Spray Pyrolysis and Their Applications in Energy Storage and Conversion. *Chem. Soc. Rev.* **2019**, *48*, 3015−3072.

(8) Tarascon, J.-M.; Armand, M. Issues and Challenges Facing Rechargeable Lithium Batteries. *Nature* **2001**, *414*, 359−367.

(9) Ji, L.; Lin, Z.; Alcoutlabi, M.; Zhang, X. Recent Developments in Nanostructured Anode Materials for Rechargeable Lithium-Ion Batteries. *Energy Environ. Sci.* **2011**, *4*, 2682.

(10) Radin, M. D.; Hy, S.; Sina, M.; Fang, C.; Liu, H.; Vinckeviciute, J.; Zhang, M.; Whittingham, M. S.; Meng, Y. S.; Van der Ven, A.

Narrowing the Gap between Theoretical and Practical Capacities in Li-Ion Layered Oxide Cathode Materials. *Adv. Energy Mater.* **2017**, *7*, 1602888.
(11) Hy, S.; Liu, H.; Zhang, M.; Qian, D.; Hwang, B.-J.; Meng, Y. S. Performance and Design Considerations for Lithium Excess Layered Oxide Positive Electrode Materials for Lithium Ion Batteries. *Energy Environ. Sci.* **2016**, *9*, 1931−1954.
(12) Li, Q.; Zhao, Y.; Liu, H.; Xu, P.; Yang, L.; Pei, K.; Zeng, Q.; Feng, Y.; Wang, P.; Che, R. Dandelion-Like Mn/Ni Co-Doped CoO/C Hollow Microspheres with Oxygen Vacancies for Advanced Lithium Storage. *ACS Nano* **2019**, *13*, 11921−11934.
(13) Zhang, H.; Zhou, L.; Noonan, O.; Martin, D. J.; Whittaker, A. K.; Yu, C. Tailoring the Void Size of Iron Oxide@Carbon Yolk-Shell Structure for Optimized Lithium Storage. *Adv. Funct. Mater.* **2014**, *24*, 4337−4342.
(14) Zhao, Y.; Li, X.; Yan, B.; Xiong, D.; Li, D.; Lawes, S.; Sun, X. Recent Developments and Understanding of Novel Mixed Transition-Metal Oxides as Anodes in Lithium Ion Batteries. *Adv. Energy Mater.* **2016**, *6*, 1502175.
(15) Bai, J.; Xi, B.; Mao, H.; Lin, Y.; Ma, X.; Feng, J.; Xiong, S. One-Step Construction of N, P-Codoped Porous Carbon Sheets/CoP Hybrids with Enhanced Lithium and Potassium Storage. *Adv. Mater.* **2018**, *30*, 1802310.
(16) Wu, C.; Kopold, P.; van Aken, P. A.; Maier, J.; Yu, Y. High Performance Graphene/Ni_2P Hybrid Anodes for Lithium and Sodium Storage through 3D Yolk-Shell-Like Nanostructural Design. *Adv. Mater.* **2017**, *29*, 1604015.
(17) Jiang, J.; Li, Y.; Liu, J.; Huang, X.; Yuan, C.; Lou, X. W. Recent Advances in Metal Oxide-Based Electrode Architecture Design for Electrochemical Energy Storage. *Adv. Mater.* **2012**, *24*, 5166−5180.
(18) Wang, Z.; Zhou, L.; Lou, X. W. Metal Oxide Hollow Nanostructures for Lithium-Ion Batteries. *Adv. Mater.* **2012**, *24*, 1903−1911.
(19) Yan, S.; Abhilash, K. P.; Tang, L.; Yang, M.; Ma, Y.; Xia, Q.; Guo, Q.; Xia, H. Research Advances of Amorphous Metal Oxides in Electrochemical Energy Storage and Conversion. *Small* **2018**, *15*, 1804371.
(20) Lu, Y.; Yu, L.; Lou, X. W. Nanostructured Conversion-Type Anode Materials for Advanced Lithium-Ion Batteries. *Chem.* **2018**, *4*, 972−996.
(21) Mahmood, N.; Tang, T.; Hou, Y. Nanostructured Anode Materials for Lithium Ion Batteries: Progress, Challenge and Perspective. *Adv. Energy Mater.* **2016**, *6*, 1600374.
(22) Deng, J.; Yu, X.; Qin, X.; Zhou, D.; Zhang, L.; Duan, H.; Kang, F.; Li, B.; Wang, G. Co-B Nanoflakes as Multifunctional Bridges in $ZnCo_2O_4$ Micro-/Nanospheres for Superior Lithium Storage with Boosted Kinetics and Stability. *Adv. Energy Mater.* **2019**, *9*, 1803612.
(23) Hao, J.; Zhang, J.; Xia, G.; Liu, Y.; Zheng, Y.; Zhang, W.; Tang, Y.; Pang, W. K.; Guo, Z. Heterostructure Manipulation *via In Situ* Localized Phase Transformation for High-Rate and Highly Durable Lithium Ion Storage. *ACS Nano* **2018**, *12*, 10430−10438.
(24) Yu, X.-Y.; Yu, L.; Lou, X. W. Metal Sulfide Hollow Nanostructures for Electrochemical Energy Storage. *Adv. Energy Mater.* **2016**, *6*, 1501333.
(25) Yu, X. Y.; Lou, X. W. Mixed Metal Sulfides for Electrochemical Energy Storage and Conversion. *Adv. Energy Mater.* **2018**, *8*, 1701592.
(26) Liu, H.; Su, D.; Zhou, R.; Sun, B.; Wang, G.; Qiao, S. Z. Highly Ordered Mesoporous MoS_2 with Expanded Spacing of the (002) Crystal Plane for Ultrafast Lithium Ion Storage. *Adv. Energy Mater.* **2012**, *2*, 970−975.
(27) Kim, M. G.; Cho, J. Reversible and High-Capacity Nanostructured Electrode Materials for Li-Ion Batteries. *Adv. Funct. Mater.* **2009**, *19*, 1497−1514.
(28) Liu, W.; Zhi, H.; Yu, X. Recent Progress in Phosphorus Based Anode Materials for Lithium/Sodium Ion Batteries. *Energy Storage Mater.* **2019**, *16*, 290−322.
(29) Chen, Y.; Zhang, W.; Zhou, D.; Tian, H.; Su, D.; Wang, C.; Stockdale, D.; Kang, F.; Li, B.; Wang, G. Co-Fe Mixed Metal Phosphide Nanocubes with Highly Interconnected-Pore Architecture as an Efficient Polysulfide Mediator for Lithium-Sulfur Batteries. *ACS Nano* **2019**, *13*, 4731−4741.
(30) Hou, B. H.; Wang, Y. Y.; Ning, Q. L.; Fan, C. Y.; Xi, X. T.; Yang, X.; Wang, J.; Zhang, J. P.; Wang, X.; Wu, X. L. An FeP@C Nanoarray Vertically Grown on Graphene Nanosheets: An Ultrastable Li-Ion Battery Anode with Pseudocapacitance-Boosted Electrochemical Kinetics. *Nanoscale* **2019**, *11*, 1304−1312.
(31) Wang, X.; Chen, K.; Wang, G.; Liu, X.; Wang, H. Rational Design of Three-Dimensional Graphene Encapsulated with Hollow FeP@Carbon Nanocomposite as Outstanding Anode Material for Lithium Ion and Sodium Ion Batteries. *ACS Nano* **2017**, *11*, 11602−11616.
(32) Carenco, S.; Portehault, D.; Boissiere, C.; Mezailles, N.; Sanchez, C. Nanoscaled Metal Borides and Phosphides: Recent Developments and Perspectives. *Chem. Rev.* **2013**, *113*, 7981−8065.
(33) Chen, J.; Fan, X.; Ji, X.; Gao, T.; Hou, S.; Zhou, X.; Wang, L.; Wang, F.; Yang, C.; Chen, L.; Wang, C. Intercalation of Bi Nanoparticles into Graphite Results in an Ultra-Fast and Ultra-Stable Anode Material for Sodium-Ion Batteries. *Energy Environ. Sci.* **2018**, *11*, 1218−1225.
(34) Yang, F.; Gao, H.; Hao, J.; Zhang, S.; Li, P.; Liu, Y.; Chen, J.; Guo, Z. Yolk-Shell Structured FeP@C Nanoboxes as Advanced Anode Materials for Rechargeable Lithium-/Potassium-Ion Batteries. *Adv. Funct. Mater.* **2019**, *29*, 1808291.
(35) Wu, S.; Fu, G.; Lv, W.; Wei, J.; Chen, W.; Yi, H.; Gu, M.; Bai, X.; Zhu, L.; Tan, C.; Liang, Y.; Zhu, G.; He, J.; Wang, X.; Zhang, K. H. L.; Xiong, J.; He, W. A Single-Step Hydrothermal Route to 3D Hierarchical Cu_2O/CuO/rGO Nanosheets as High-Performance Anode of Lithium-Ion Batteries. *Small* **2018**, *14*, 1702667.
(36) Yuan, H.; Wu, M.; Zheng, J.; Chen, Z. G.; Zhang, W.; Luo, J.; Jin, C.; Sheng, O.; Liang, C.; Gan, Y.; Xia, Y.; Zhang, J.; Huang, H.; Liu, Y.; Nai, J.; Tao, X. Empowering Metal Phosphides Anode with Catalytic Attribute toward Superior Cyclability for Lithium-Ion Storage. *Adv. Funct. Mater.* **2019**, *29*, 1809051.
(37) Shi, S.; Li, Z.; Sun, Y.; Wang, B.; Liu, Q.; Hou, Y.; Huang, S.; Huang, J.; Zhao, Y. A Covalent Heterostructure of Monodisperse Ni_2P Immobilized on N, P-Co-Doped Carbon Nanosheets for High Performance Sodium/Lithium Storage. *Nano Energy* **2018**, *48*, 510−517.
(38) Dong, C.; Guo, L.; He, Y.; Chen, C.; Qian, Y.; Chen, Y.; Xu, L. Sandwich-Like Ni_2P Nanoarray/Nitrogen-Doped Graphene Nanoarchitecture as a High-Performance Anode for Sodium and Lithium Ion Batteries. *Energy Storage Mater.* **2018**, *15*, 234−241.
(39) Liu, X.; Li, W.; Zhao, X.; Liu, Y.; Nan, C. W.; Fan, L. Z. Two Birds with One Stone: Metal-Organic Framework Derived Micro-/Nanostructured Ni_2P/Ni Hybrids Embedded in Porous Carbon for Electrocatalysis and Energy Storage. *Adv. Funct. Mater.* **2019**, *29*, 1901510.
(40) Liu, H.; Liu, X.; Li, W.; Guo, X.; Wang, Y.; Wang, G.; Zhao, D. Porous Carbon Composites for Next Generation Rechargeable Lithium Batteries. *Adv. Energy Mater.* **2017**, *7*, 1700283.
(41) Li, W.; Ke, L.; Wei, Y.; Guo, S.; Gan, L.; Li, H.; Zhai, T.; Zhou, H. Highly Reversible Sodium Storage in a GeP_5/C Composite Anode with Large Capacity and Low Voltage. *J. Mater. Chem. A* **2017**, *5*, 4413−4420.
(42) Li, W.; Yu, J.; Wen, J.; Liao, J.; Ye, Z.; Zhao, B.; Li, X.; Zhang, H.; Liu, M.; Guo, Z. An Amorphous ZnP/Graphite Composite with Chemical Bonding for Ultra-Reversible Lithium Storage. *J. Mater. Chem. A* **2019**, *7*, 16785−16792.
(43) Gao, H.; Yang, F.; Zheng, Y.; Zhang, Q.; Hao, J.; Zhang, S.; Zheng, H.; Chen, J.; Liu, H.; Guo, Z. Three-Dimensional Porous Cobalt Phosphide Nanocubes Encapsulated in a Graphene Aerogel as an Advanced Anode with High Coulombic Efficiency for High-Energy Lithium-Ion Batteries. *ACS Appl. Mater. Interfaces* **2019**, *11*, 5373−5379.
(44) Zhang, W.; Mao, J.; Li, S.; Chen, Z.; Guo, Z. Phosphorus-Based Alloy Materials for Advanced Potassium-Ion Battery Anode. *J. Am. Chem. Soc.* **2017**, *139*, 3316−3319.

https://dx.doi.org/10.1021/acsnano.9b08575
ACS Nano 2020, 14, 9545−9561

(45) Liu, J.; Kopold, P.; Wu, C.; van Aken, P. A.; Maier, J.; Yu, Y. Uniform Yolk-Shell Sn_4P_3@C Nanospheres as High-Capacity and Cycle-Stable Anode Materials for Sodium-Ion Batteries. *Energy Environ. Sci.* **2015**, *8*, 3531−3538.
(46) Wu, F.; Srot, V.; Chen, S.; Lorger, S.; van Aken, P. A.; Maier, J.; Yu, Y. 3D Honeycomb Architecture Enables a High-Rate and Long-Life Iron (III) Fluoride-Lithium Battery. *Adv. Mater.* **2019**, *31*, 1905146.
(47) Xiong, P.; Bai, P.; Tu, S.; Cheng, M.; Zhang, J.; Sun, J.; Xu, Y. Red Phosphorus Nanoparticle@3D Interconnected Carbon Nanosheet Framework Composite for Potassium-Ion Battery Anodes. *Small* **2018**, *14*, 1802140.
(48) Wang, M.; Yang, Z.; Li, W.; Gu, L.; Yu, Y. Superior Sodium Storage in 3D Interconnected Nitrogen and Oxygen Dual-Doped Carbon Network. *Small* **2016**, *12*, 2559−2566.
(49) Shi, J.; Wang, Z.; Fu, Y. Q. Density Functional Theory Study of Lithium Diffusion at the Interface between Olivine-Type $LiFePO_4$ and $LiMnPO_4$. *J. Phys. D: Appl. Phys.* **2016**, *49*, 505601.
(50) Zheng, Y.; Zhou, T.; Zhao, X.; Pang, W. K.; Gao, H.; Li, S.; Zhou, Z.; Liu, H.; Guo, Z. Atomic Interface Engineering and Electric-Field Effect in Ultrathin Bi_2MoO_6 Nanosheets for Superior Lithium Ion Storage. *Adv. Mater.* **2017**, *29*, 1700396.
(51) Zhao, L.; Wu, H. H.; Yang, C.; Zhang, Q.; Zhong, G.; Zheng, Z.; Chen, H.; Wang, J.; He, K.; Wang, B.; Zhu, T.; Zeng, X. C.; Liu, M.; Wang, M. S. Mechanistic Origin of the High Performance of Yolk@Shell Bi_2S_3@N-Doped Carbon Nanowire Electrodes. *ACS Nano* **2018**, *12*, 12597−12611.
(52) Han, F.; Zhang, C.; Yang, J.; Ma, G.; He, K.; Li, X. Well-Dispersed and Porous FeP@C Nanoplates with Stable and Ultrafast Lithium Storage Performance through Conversion Reaction Mechanism. *J. Mater. Chem. A* **2016**, *4*, 12781−12789.
(53) Wang, Y.; Fu, Q.; Li, C.; Li, H.; Tang, H. Nitrogen and Phosphorus Dual-Doped Graphene Aerogel Confined Monodisperse Iron Phosphide Nanodots as an Ultrafast and Long-Term Cycling Anode Material for Sodium-Ion Batteries. *ACS Sustainable Chem. Eng.* **2018**, *6*, 15083−15091.
(54) Pu, Z.; Amiinu, I. S.; Zhang, C.; Wang, M.; Kou, Z.; Mu, S. Phytic Acid-Derivative Transition Metal Phosphides Encapsulated in N, P-Codoped Carbon: An Efficient and Durable Hydrogen Evolution Electrocatalyst in a Wide PH Range. *Nanoscale* **2017**, *9*, 3555−3560.
(55) Zhu, P.; Zhang, Z.; Hao, S.; Zhang, B.; Zhao, P.; Yu, J.; Cai, J.; Huang, Y.; Yang, Z. Multi-Channel FeP@C Octahedra Anchored on Reduced Graphene Oxide Nanosheet with Efficient Performance for Lithium-Ion Batteries. *Carbon* **2018**, *139*, 477−485.
(56) Wang, R.; Dong, X.-Y.; Du, J.; Zhao, J.-Y.; Zang, S.-Q. MOF-Derived Bifunctional Cu_3P Nanoparticles Coated by a N, P-Codoped Carbon Shell for Hydrogen Evolution and Oxygen Reduction. *Adv. Mater.* **2018**, *30*, 1703711.
(57) Guang, Z.; Huang, Y.; Chen, X.; Sun, X.; Wang, M.; Feng, X.; Chen, C.; Liu, X. Three-Dimensional P-Doped Carbon Skeleton with Built-In Ni_2P Nanospheres as Efficient Polysulfides Barrier for High-Performance Lithium-Sulfur Batteries. *Electrochim. Acta* **2019**, *307*, 260−268.
(58) Huang, L.; Cao, X.; Pan, A.; Chen, J.; Kong, X.; Yang, Y.; Liang, S.; Cao, G. Bimetallic Phosphides Embedded in Hierarchical P-Doped Carbon for Sodium Ion Battery and Hydrogen Evolution Reaction Applications. *Sci. China Mater.* **2019**, *62*, 1857−1867.
(59) Pan, D.; Wang, S.; Zhao, B.; Wu, M.; Zhang, H.; Wang, Y.; Jiao, Z. Li Storage Properties of Disordered Graphene Nanosheets. *Chem. Mater.* **2009**, *21*, 3136−3142.
(60) Zheng, Z.; Li, P.; Huang, J.; Liu, H.; Zao, Y.; Hu, Z.; Zhang, L.; Chen, H.; Wang, M.-S.; Peng, D.-L.; Zhang, Q. High Performance Columnar-Like Fe_2O_3@Carbon Composite Anode *via* Yolk@Shell Structural Design. *J. Energy Chem.* **2020**, *41*, 126−134.
(61) Wu, C.; Maier, J.; Yu, Y. Generalizable Synthesis of Metal-Sulfides/Carbon Hybrids with Multiscale, Hierarchically Ordered Structures as Advanced Electrodes for Lithium Storage. *Adv. Mater.* **2016**, *28*, 174−180.
(62) Yu, J.; Wang, Y.; Kong, L.; Chen, S.; Zhang, S. Neuron-Mimic Smart Electrode: A Two-Dimensional Multiscale Synergistic Strategy for Densely Packed and High-Rate Lithium Storage. *ACS Nano* **2019**, *13*, 9148−9160.
(63) Zhao, K.; Wen, M.; Dong, Y.; Zhang, L.; Yan, M.; Xu, W.; Niu, C.; Zhou, L.; Wei, Q.; Ren, W.; Wang, X.; Mai, L. Thermal Induced Strain Relaxation of 1D Iron Oxide for Solid Electrolyte Interphase Control and Lithium Storage Improvement. *Adv. Energy Mater.* **2017**, *7*, 1601582.
(64) Tang, C.; Liu, Y.; Xu, C.; Zhu, J.; Wei, X.; Zhou, L.; He, L.; Yang, W.; Mai, L. Ultrafine Nickel-Nanoparticle-Enabled SiO_2 Hierarchical Hollow Spheres for High-Performance Lithium Storage. *Adv. Funct. Mater.* **2018**, *28*, 1704561.
(65) Kennedy, T.; Brandon, M.; Ryan, K. M. Advances in the Application of Silicon and Germanium Nanowires for High-Performance Lithium-Ion Batteries. *Adv. Mater.* **2016**, *28*, 5696−5704.
(66) Zhao, J.; Lu, Z.; Liu, N.; Lee, H. W.; McDowell, M. T.; Cui, Y. Dry-Air-Stable Lithium Silicide-Lithium Oxide Core-Shell Nanoparticles as High-Capacity Prelithiation Reagents. *Nat. Commun.* **2014**, *5*, 5088.
(67) Xiao, Q.; Gu, M.; Yang, H.; Li, B.; Zhang, C.; Liu, Y.; Liu, F.; Dai, F.; Yang, L.; Liu, Z.; Xiao, X.; Liu, G.; Zhao, P.; Zhang, S.; Wang, C.; Lu, Y.; Cai, M. Inward Lithium-Ion Breathing of Hierarchically Porous Silicon Anodes. *Nat. Commun.* **2015**, *6*, 8844.
(68) Chen, J.; Mao, Z.; Zhang, L.; Wang, D.; Xu, R.; Bie, L.; Fahlman, B. D. Nitrogen-Deficient Graphitic Carbon Nitride with Enhanced Performance for Lithium Ion Battery Anodes. *ACS Nano* **2017**, *11*, 12650−12657.
(69) Wang, X.; Weng, Q.; Liu, X.; Wang, X.; Tang, D. M.; Tian, W.; Zhang, C.; Yi, W.; Liu, D.; Bando, Y.; Golberg, D. Atomistic Origins of High Rate Capability and Capacity of N-Doped Graphene for Lithium Storage. *Nano Lett.* **2014**, *14*, 1164−1171.
(70) Kesavan, T.; Partheeban, T.; Vivekanantha, M.; Prabu, N.; Kundu, M.; Selvarajan, P.; Umapathy, S.; Vinu, A.; Sasidharan, M. Design of P-Doped Mesoporous Carbon Nitrides as High-Performance Anode Materials for Li-Ion Battery. *ACS Appl. Mater. Interfaces* **2020**, *12*, 24007−24018.
(71) Sun, H.; Xin, G.; Hu, T.; Yu, M.; Shao, D.; Sun, X.; Lian, J. High-Rate Lithiation-Induced Reactivation of Mesoporous Hollow Spheres for Long-Lived Lithium-Ion Batteries. *Nat. Commun.* **2014**, *5*, 4526.
(72) Lian, Q.; Zhou, G.; Liu, J.; Wu, C.; Wei, W.; Chen, L.; Li, C. Extrinsic Pseudocapacitve Li-Ion Storage of SnS Anode *via* Lithiation-Induced Structural Optimization on Cycling. *J. Power Sources* **2017**, *366*, 1−8.
(73) Sun, X.; Yan, C.; Chen, Y.; Si, W.; Deng, J.; Oswald, S.; Liu, L.; Schmidt, O. G. Three-Dimensionally "Curved" NiO Nanomembranes as Ultrahigh Rate Capability Anodes for Li-Ion Batteries with Long Cycle Lifetimes. *Adv. Energy Mater.* **2014**, *4*, 1300912.
(74) He, H.; Fu, W.; Wang, H.; Wang, H.; Jin, C.; Fan, H. J.; Liu, Z. Silica-Modified SnO_2-Graphene "Slime" for Self-Enhanced Li-Ion Battery Anode. *Nano Energy* **2017**, *34*, 449−455.
(75) Zhang, Q.; Wang, J.; Dong, J.; Ding, F.; Li, X.; Zhang, B.; Yang, S.; Zhang, K. Facile General Strategy toward Hierarchical Mesoporous Transition Metal Oxides Arrays on Three-Dimensional Macroporous Foam with Superior Lithium Storage Properties. *Nano Energy* **2015**, *13*, 77−91.
(76) An, Q.; Lv, F.; Liu, Q.; Han, C.; Zhao, K.; Sheng, J.; Wei, Q.; Yan, M.; Mai, L. Amorphous Vanadium Oxide Matrixes Supporting Hierarchical Porous Fe_3O_4/Graphene Nanowires as a High-Rate Lithium Storage Anode. *Nano Lett.* **2014**, *14*, 6250−6256.
(77) Li, Y.; Huang, Y.; Zheng, Y.; Huang, R.; Yao, J. Facile and Efficient Synthesis of α-Fe_2O_3 Nanocrystals by Glucose-Assisted Thermal Decomposition Method and Its Application in Lithium Ion Batteries. *J. Power Sources* **2019**, *416*, 62−71.
(78) Zhao, K.; Liu, F.; Niu, C.; Xu, W.; Dong, Y.; Zhang, L.; Xie, S.; Yan, M.; Wei, Q.; Zhao, D.; Mai, L. Graphene Oxide Wrapped Amorphous Copper Vanadium Oxide with Enhanced Capacitive

https://dx.doi.org/10.1021/acsnano.9b08575
ACS Nano 2020, 14, 9545−9561

Behavior for High-Rate and Long-Life Lithium-Ion Battery Anodes. *Adv. Sci.* **2015**, *2*, 1500154.
(79) Chen, C.; Wen, Y.; Hu, X.; Ji, X.; Yan, M.; Mai, L.; Hu, P.; Shan, B.; Huang, Y. Na^+ Intercalation Pseudocapacitance in Graphene-Coupled Titanium Oxide Enabling Ultra-Fast Sodium Storage and Long-Term Cycling. *Nat. Commun.* **2015**, *6*, 6929.
(80) Li, B.; Xi, B.; Feng, Z.; Lin, Y.; Liu, J.; Feng, J.; Qian, Y.; Xiong, S. Hierarchical Porous Nanosheets Constructed by Graphene-Coated, Interconnected TiO_2 Nanoparticles for Ultrafast Sodium Storage. *Adv. Mater.* **2018**, *30*, 1705788.
(81) Yuan, C.; Wu, H. B.; Xie, Y.; Lou, X. W. Mixed Transition-Metal Oxides: Design, Synthesis, and Energy-Related Applications. *Angew. Chem., Int. Ed.* **2014**, *53*, 1488−1504.
(82) Zhang, Q.; Chen, H.; Luo, L.; Zhao, B.; Luo, H.; Han, X.; Wang, J.; Wang, C.; Yang, Y.; Zhu, T.; Liu, M. Harnessing the Concurrent Reaction Dynamics in Active Si and Ge to Achieve High Performance Lithium-Ion Batteries. *Energy Environ. Sci.* **2018**, *11*, 669−681.
(83) Liu, X. H.; Liu, Y.; Kushima, A.; Zhang, S.; Zhu, T.; Li, J.; Huang, J. Y. *In Situ* TEM Experiments of Electrochemical Lithiation and Delithiation of Individual Nanostructures. *Adv. Energy Mater.* **2012**, *2*, 722−741.
(84) Su, Q.; Xie, D.; Zhang, J.; Du, G.; Xu, B. *In Situ* Transmission Electron Microscopy Observation of the Conversion Mechanism of Fe_2O_3/Graphene Anode during Lithiation-Delithiation Processes. *ACS Nano* **2013**, *7*, 9115−9121.
(85) Liu, Z.; Zhang, X.; Huang, D.; Gao, B.; Ni, C.; Wang, L.; Ren, Y.; Wang, J.; Gou, H.; Wang, G. Confined Seeds Derived Sodium Titanate/Graphene Composite with Synergistic Storage Ability toward High Performance Sodium Ion Capacitors. *Chem. Eng. J.* **2020**, *379*, 122418.
(86) Yuan, K.; Sfaelou, S.; Qiu, M.; Lützenkirchen-Hecht, D.; Zhuang, X.; Chen, Y.; Yuan, C.; Feng, X.; Scherf, U. Synergetic Contribution of Boron and Fe-N_x Species in Porous Carbons toward Efficient Electrocatalysts for Oxygen Reduction Reaction. *ACS Energy. Lett.* **2018**, *3*, 252−260.
(87) Genovese, C.; Schuster, M. E.; Gibson, E. K.; Gianolio, D.; Posligua, V.; Grau-Crespo, R.; Cibin, G.; Wells, P. P.; Garai, D.; Solokha, V.; Krick Calderon, S.; Velasco-Velez, J. J.; Ampelli, C.; Perathoner, S.; Held, G.; Centi, G.; Arrigo, R. Operando Spectroscopy Study of the Carbon Dioxide Electro-Reduction by Iron Species on Nitrogen-Doped Carbon. *Nat. Commun.* **2018**, *9*, 935.
(88) Giannozzi, P.; Andreussi, O.; Brumme, T.; Bunau, O.; Buongiorno Nardelli, M.; Calandra, M.; Car, R.; Cavazzoni, C.; Ceresoli, D.; Cococcioni, M.; Colonna, N.; Carnimeo, I.; Dal Corso, A.; de Gironcoli, S.; Delugas, P.; DiStasio, R. A.; Ferretti, A.; Floris, A.; Fratesi, G.; Fugallo, G. Advanced Capabilities for Materials Modelling with Quantum ESPRESSO. *J. Phys.: Condens. Matter* **2017**, *29*, 465901.
(89) Liu, G.; Wu, H.-H.; Meng, Q.; Zhang, T.; Sun, D.; Jin, X.; Guo, D.; Wu, N.; Liu, X.; Kim, J.-K. Role of the Anatase/TiO_2(B) Heterointerface for Ultrastable High-Rate Lithium and Sodium Energy Storage Performance. *Nanoscale Horiz.* **2020**, *5*, 150−162.
(90) Wu, H. H.; Huang, H.; Zhong, J.; Yu, S.; Zhang, Q.; Zeng, X. C. Monolayer Triphosphates MP_3 (M = Sn, Ge) with Excellent Basal Catalytic Activity for Hydrogen Evolution Reaction. *Nanoscale* **2019**, *11*, 12210−12219.

https://dx.doi.org/10.1021/acsnano.9b08575
ACS Nano 2020, 14, 9545−9561